Deep Resources Engineering 3 (2026) 100237

Contents lists available at ScienceDirect

Deep Resources Engineering

journal homepage: www.keaipublishing.com/en/journals/deepre/

Full length article

Response induced by transient blasting or seismic P-wave around a diversion tunnel with an imperfect rock-liner interface

Wanquan Mei [a,b], Peng-Zhi Pan [a,b,*], Amin Hekmatnejad [c], Zhaofeng Wang [a,b], Yi Xie [a,b,d], Qingsong Zheng [a,b]

[a] State Key Laboratory of Geomechanics and Geotechnical Engineering Safety, Institute of Rock and Soil Mechanics, Chinese Academy of Sciences, Wuhan 430071, China
[b] University of Chinese Academy of Sciences, Beijing 100049, China
[c] Departamento de Ingeniería de Minería, Escuela de Ingeniería, Pontificia Universidad Católica de Chile, Santiago, Chile
[d] State Key Laboratory of Intelligent Deep Metal Mining and Equipment, Northeastern University, Shenyang 110819, China

ARTICLE INFO

Keywords:
Transient response
Spring interface model
Numerical inverse algorithm
Dynamic stress concentration

ABSTRACT

The work focuses on transient response of a deep-buried circular lined diversion tunnel with an imperfect rock-liner interface, which is full of water, subjected to an aperiodic blasting or seismic P-wave in a full space. Laplace transform was first applied to governing equations in rock mass, liner and water to obtain the frequency-domain expressions of wave fields in various media under planar blasting or seismic P-wave. Furthermore, a spring interface model was adopted to describe rock mass-liner imperfect characteristics. Laplace transformation was performed for the imperfect rock mass-liner and perfect liner-fluid boundary conditions to determine complex coefficients of wave fields in the frequency domain. Ultimately, corresponding time-domain solutions triggered by the planar blasting or seismic P-wave were evaluated by numerical inverse algorithm. Limitation analyses including a deep-buried empty cavity and a lined counterpart verified the proposed method under triangular P-wave excitation. The theoretical results indicated that the scopes perpendicular to the perturbation direction generated pronounced dynamic tensile or compressive stress concentration under the blasting or seismic P-wave. The rock mass-liner contact state had a significant influence on the transient response of surrounding rock, liner and water and the effect of radial elastic coefficient on dynamic response was more sensitive than that of hoop counterpart, especially in fluid. The existence of fluid promoted the interaction between the stress wave and the lined tunnel, resulting in more remarkable fluctuations of time-domain response. These results can provide a theoretical basis for the earthquake resistant design and support of diversion tunnel.

1. Introduction

Deep-buried diversion tunnels, essential components of major hydropower and water conveyance projects, are frequently constructed in complex geological environments characterized by high geo-stress. During their long service life, these underground structures are inevitably subjected to transient dynamic perturbations, stemming from various sources, including production blasting in excavations, seismic events and other human-induced vibrations [1,2]. Unlike harmonic waves, these real-world perturbations are characterized by transient and aperiodic variations, short durations and broad frequency spectra [3,4]. The superposition of aforementioned dynamic loads onto the pre-existing high static stress fields results in challenging mechanical environment for diversion tunnel stability. Practical engineering case studies have revealed that strong disturbance can trigger severe damage and failure in diversion tunnels, manifesting as concrete spalling, lining cracks, rockburst of surrounding rock and collapse [2,5]. Thus, it is importance to investigate the scattering mechanism triggered by stress disturbance and transient wave-induced response around a deep-buried diversion tunnel.

Extensive investigations have focused on the steady-state dynamic response of deep-buried single or twin tunnels and roadways subjected to harmonically time-varying waves. The foundational work in this field frequently employs the wave function expansion method (WFEM). This method was pioneered by Mow and Pao [6] for analyzing the dynamic stress concentration around an empty cavity subjected to P-, SV- and

* Corresponding author at: State Key Laboratory of Geomechanics and Geotechnical Engineering Safety, Institute of Rock and Soil Mechanics, Chinese Academy of Sciences, Wuhan 430071, China.
E-mail address: pzpan@whrsm.ac.cn (P.-Z. Pan).

https://doi.org/10.1016/j.deepre.2026.100237
Received 21 July 2025; Received in revised form 5 January 2026; Accepted 12 January 2026
Available online 13 January 2026

SH-waves in a full space. Based on the work presented by Mow and Pao [6], subsequent investigations utilized WFEM to explore the scattering and diffraction of elastic waves by various configurations, including single lined tunnel, twin unlined tunnels or twin lined counterparts [7–12]. A critical aspect of modelling lined tunnels was the characterization of the rock mass-liner interface. Many analytical models assumed a perfect contact interface, where displacement and stress components were continuous across the rock mass-liner boundary [12]. However, this idealization frequently contradicted practical engineering. To address this, some scholars proposed imperfect rock mass-liner contact interface models to account for potential discontinuities caused by factors such as waterproof board, uneven surfaces, or pre-existing geological features like foliation, micro-cracks, faults and joints [7,8,10,11]. These investigations highlight that such imperfection remarkably alter dynamic stress distributions and become potential damage and failure initiation zones. WFEM is powerful, while it is inherently limited to conventional geometries like circles and ellipses. To solve the scattering and diffraction by arbitrary cross-sections in a full space, the combination of complex function method (CFM) and conformal mapping technique was proposed [13]. Based on the investigation conducted by Liu et al. [13], scattering and diffraction of P-wave by an elliptic cross-section, straight-wall arched tunnel and composite lined horseshoe tunnel were analyzed [14–17]. Moreover, some numerical schemes were also adopted to investigate the scattering and diffraction of harmonic waves by underground tunnels. Liu et al. [18] utilized indirect boundary element method (IBEM) to analyze the dynamic interaction between a shallow-buried liner tunnel and a hill subjected to in-plane SV-wave. Xu et al. [19] employed indirect boundary integral element method (IBIEM) to investigate the diffraction and scattering of Rayleigh waves by two shallow-buried tunnels and the effects of porosity, incident frequency and cavity spacing on the surface displacement and stress distribution around the cavities were discussed. Yang et al. [20] used finite-infinite element method to analyze the scattering of harmonic P- and SV-waves by a shallow-buried circular cavity. It is crucial to note that the aforementioned references focus on the dynamic response triggered by harmonic SH-, SV- and P-waves under specific frequency. In contrast, the real-world disturbances from blasting or earthquakes are predominantly transient and aperiodic in nature. The dynamic response mechanisms differ from the well-studied harmonic case. Therefore, it is necessary to investigate the dynamic response induced by the aperiodic time-varying load.

For the theoretical transient analysis, methods such as the combination of the Fourier synthesis technique with the Duhamel integral method (FST-DIM), the combination of the Fourier synthesis technique with domain transformation and numerical inversion (FST-DT-NI) and the combination of integral transform with numerical inversion (IT-NI) have been widely employed to investigate the dynamic time-history response, spatiotemporal evolutions of stress and velocity around tunnels in a half or full space [21–28]. Using FST-DIM, Tao et al. [23] and Li et al. [29] presented the dynamic stress concentration and velocity vibration around an circular empty cavity subjected to triangular or needle load and the effects of ratio of wavelength to diameter, waveform and physical parameters of the rock mass were explored. Moreover, based on FST-DIM, the transient response of twin lined tunnels with imperfect rock mass-liner interfaces under horizontal disturbance was investigated and the effects of center-to-center distance between twin tunnels, radial and hoop elastic coefficients of the imperfect rock mass-liner interfaces were explored [30]. By applying FST-DT-NI, the transient response of a shallow lined tunnel was analyzed and the influences of embedment depth, incident angle and rock mass-liner interface state on the dynamic stress concentration and velocity vibration were discussed [26]. Using IT-NI, the transient response of a lined tunnel with imperfect rock mass-liner interface was obtained and the effects of interface coefficients and liner thickness were analyzed [27, 28]. Regarding the transient response of fluid-filled tunnels, Tao et al. [31] and Li et al. [21] employed FST-DIM to analyze the effects of the fluid, Poisson's ratio of rock mass and rock mass-liner interface contact state on dynamic response. Using a combination of WFEM, modified Graf's addition theorem, Fourier synthesis approach and Duhamel integral, Mei et al. [32] analyzed the scattering and diffraction of triangular blasting P- and SV-waves by twin lined diversion tunnels with imperfect rock mass-liner interfaces in a full space and the effects of disturbance direction, tunnel spacing, ratio of tunnel radius and rock mass-liner interface state on the dynamic response of surrounding rock, liner and water were presented. However, it should be noted that the aforementioned transient response of a single or multiple tunnels are evaluated by simplifying the disturbance function as triangular load [29, 30], Ricker-wavelet waveform [33–36], half-sine waveform [37,38] or needle counterpart [39]. These simplifications fail to accurately characterize the variations of complex perturbation load and evaluate the theoretical dynamic response triggered by intricate disturbance. Therefore, it is necessary to investigate the dynamic response of fluid-filled lined tunnel with imperfect rock mass-liner interface subjected to an arbitrary disturbance waveform.

This paper focuses on the transient response of a fluid-filled diversion tunnel with an imperfect rock mass-liner interface subjected to planar blasting or seismic P-wave in a full space. The frequency-domain solutions around the fluid-filled lined tunnel with an imperfect rock mass-liner interface were first derived analytically using integral transform techniques. These solutions were subsequently inverted into the time-domain results via numerical inversion of Laplace transform. The validity and accuracy of the proposed method were established by degenerating the present model to specific cases and comparing the results with the existing theoretical and numerical benchmarks from references. Ultimately, the effects of elastic modulus of surrounding rock, elastic coefficients of the imperfect interface and waveform under planar blasting or seismic P-wave were discussed in detail.

2. Frequency-domain and time-domain solutions of diversion tunnel

2.1. Computational model and incident wave field in the frequency domain

It is assumed that an infinite circular lined diversion tunnel is embedded in a full-space rock mass and that the disturbance direction is perpendicular to the tunnel axis. Both the rock mass and liner are homogeneous, elastic and isotropic, characterized by the mass density ρ_l, Lame's constants λ_l and μ_l (l=1,2), where subscript l= 1 and l= 2 denote the rock mass and liner, respectively. The water is treated as an ideal compressible and inviscid fluid, whose physical parameters are defined by bulk modulus K_w and mass density ρ_w. Based on the preceding assumptions, the computational model subjected to blasting or seismic dynamic disturbance is simplified as plane strain problem, as demonstrated in Fig. 1. Inner and outer radii of the liner are a and b, respectively. A Cartesian coordinate (x, y) with origin at the tunnel center and corresponding polar counterpart (r, θ) are introduced to describe the incident and scattered wave fields as well as boundary conditions in both the frequency and time domains.

When a time-domain function $f_1(t)$ is characterized by $f_1(t) = 0$ for $t < 0$ and defined in the time-domain interval $[0, +\infty)$, the Laplace transformation of the time-domain function is represented by

$$\overline{f_1}(s) = \int_0^{+\infty} f_1(t)\mathrm{e}^{-st}\mathrm{d}t \tag{1}$$

where s denotes the Laplace transformation parameter.

In practical engineering, the disturbance load induced by blasting excavation or earthquake is frequently characterized by sampled or tabulated functions with finite time points. The Laplace transform requires the overall variation of the function over the entire semi-infinite time domain $[0, +\infty)$, while the sampled data recorded by blasting vibration meter or seismometer are frequently available over a finite interval. Therefore, appropriate extrapolation to infinity is conducted to evaluate the Laplace transformation of the sampled or tabulated data. In general, the initial value of sampled data is characterized by zero and the sampling frequency is known in the range $[0, t_N]$, while extrapolation is required in the range $[t_N, +\infty)$. To obtain the various function approximations at the adjacent two endpoints, the Laplace transformation of the perturbation load is represented by

$$\overline{f_1}(s) = \int_0^{t_1} f_1(t)e^{-st}dt + \int_{t_1}^{t_N} f_1(t)e^{-st}dt + \int_{t_N}^{+\infty} f_1(t)e^{-st}dt \tag{2}$$

Here a piecewise-linear interpolation is employed to construct a continuous function from the sampled data for evaluating these integrals. For the third integral mentioned above, it is assumed that the value of sampled data is zero when time variable exceeds t_{N+1}. Substituting the piecewise linear approximation into Eq.(2), the Laplace transform simplifies

$$\overline{f_1}(s) = \frac{P_0}{s}e^{-st_0} + \sum_{j=0}^{N-1} d_i \frac{P_{j+1}(e^{-st_j} - e^{-st_{j+1}})}{s^2} - \frac{P_N}{s}e^{-st_N} \tag{3}$$

where $d_i = \frac{P_{j+1}-P_j}{t_{j+1}-t_j}$ denotes the slop between adjacent sampling points. P_j represents the sampled value at time t_j.

When the distance from the wavefront of the disturbance P-wave to the tunnel center O equals to d, time is initialized. Applying the Laplace transformation to the disturbance load, the frequency-domain expression of the incident wave is expressed as

$$\overline{\phi^{(i)}} = e^{-s\frac{x+d}{C_{1p}}}\overline{f_1}(s) \tag{4}$$

where $C_{1p} = \sqrt{(\lambda_1 + 2\mu_1)/\rho_1}$ denotes the longitudinal wave velocity in the rock mass. Using the cylindrical coordinate system, Eq.(4) is further expanded into the series form

$$\overline{\phi^{(i)}} = e^{-\bar{k}_{1p}d}\overline{f_1}(s)\sum_{n=0}^{\infty}(-1)^n \varepsilon_n I_n(\bar{k}_{1p}r)\cos n\theta \tag{5}$$

where $I_n(\bullet)$ denotes the modified Bessel function of the first category with order n. $\bar{k}_{1p} = s/C_{1p}$ stands for wavenumber of longitudinal wave in the Laplace domain. ε_n is the Neumann factor ($\varepsilon_0 = 1$, $\varepsilon_n = 2$ for $n \geq 1$), consistent with cylindrical wave expansion conventions.

2.2. Frequency-domain solutions of wave equations in the rock mass and liner

Neglecting the effect of body traction, the motive equation for elastic waves in the rock mass and liner is written as

$$\mu_l \nabla^2 \boldsymbol{u}_l + (\lambda_l + \mu_l)\nabla\nabla \bullet \boldsymbol{u}_l = \rho_l \frac{\partial^2 \boldsymbol{u}_l}{\partial t^2} \tag{6}$$

where ∇^2 stands for the Laplace operator. ∇ represents the cylindrical gradient. $\boldsymbol{u}_l$ (l=1, 2) denotes the displacement vector. Based on Helmholtz decomposition principle, the displacement vector mentioned above is expressed as a combination of the gradient of a scalar potential ϕ_l with the curl of a vector potential ψ_l, represented by

$$u_l = \nabla\phi_l^{(s)} + \nabla x \psi_l^{(s)} \tag{7}$$

Substituting Eq.(7) into Eq.(6) leads to the following wave equations, given by

$$\begin{aligned} \nabla^2\phi_l^{(s)} &= \frac{1}{C_{lp}^2}\frac{\partial^2\phi_l^{(s)}}{\partial t^2} \\ \nabla^2\psi_l^{(s)} &= \frac{1}{C_{ls}^2}\frac{\partial^2\psi_l^{(s)}}{\partial t^2} \end{aligned} \tag{8}$$

where $C_{lp} = \sqrt{(\lambda_l + 2\mu_l)/\rho_l}$ and $C_{ls} = \sqrt{\mu_l/\rho_l}$ denote the longitudinal and transverse wave velocities, respectively. Applying Laplace transform to Eq.(8) leads to the following frequency-domain equations [28].

$$\begin{aligned} \frac{\partial^2\overline{\phi_l^{(s)}}}{\partial r^2} + \frac{1}{r}\frac{\partial\overline{\phi_l^{(s)}}}{\partial r} + \frac{1}{r^2}\frac{\partial^2\overline{\phi_l^{(s)}}}{\partial\theta^2} - \frac{s^2}{C_{lp}^2}\overline{\phi_l^{(s)}} = 0 \\ \frac{\partial^2\overline{\psi_l^{(s)}}}{\partial r^2} + \frac{1}{r}\frac{\partial\overline{\psi_l^{(s)}}}{\partial r} + \frac{1}{r^2}\frac{\partial^2\overline{\psi_l^{(s)}}}{\partial\theta^2} - \frac{s^2}{C_{ls}^2}\overline{\psi_l^{(s)}} = 0 \end{aligned} \tag{9}$$

The general solutions of Eq.(9) are expressed as the product of the modified Bessel functions and trigonometric functions. According to the symmetric characteristic of the computational model and the selection principle of frequency-domain potential functions, the outgoing scattered waves generated around the rock mass-liner interface in the rock mass are represented by

$$\begin{aligned} \overline{\phi_1^{(s)}} &= \sum_{n=0}^{\infty} A_{1n}K_n(\bar{k}_{1p}r)\cos n\theta \\ \overline{\psi_1^{(s)}} &= \sum_{n=0}^{\infty} B_{1n}K_n(\bar{k}_{1s}r)\sin n\theta \end{aligned} \tag{10}$$

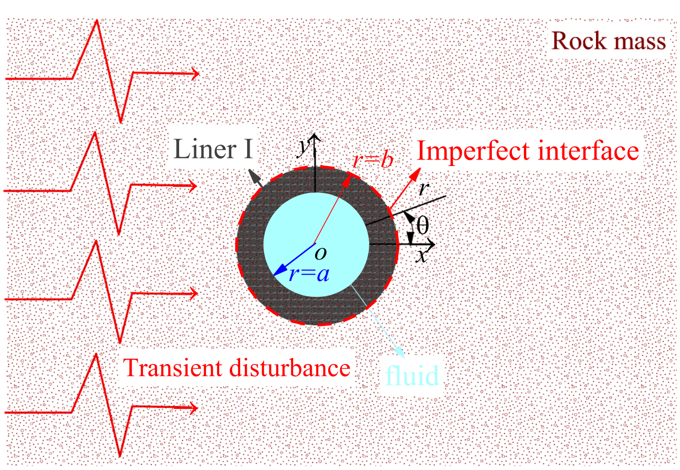

Fig. 1. The computational model of a lined diversion tunnel in a full space.

where $K_n(\bullet)$ denotes the modified Bessel function of second category with order n. $\bar{k}_{1s} = s/C_{1s}$ represents the frequency-domain wavenumber of transverse wave in rock mass. A_{1n} and B_{1n} stand for unknown complex coefficients in the frequency domain. When the incident P-wave impinges on the rock mass-liner interface, incoming scattered waves in the liner appear. At the inner boundary of the liner, outgoing scattered wave generate. Consequently, the frequency-domain displacement potentials in the liner are expressed as

$$\begin{aligned}
\overline{\phi_2^{(s)}} &= \sum_{n=0}^{\infty}\left[A_{2n}I_n(\bar{k}_{2p}r) + B_{2n}K_n(\bar{k}_{2p}r)\right]\cos n\theta \\
\overline{\psi_2^{(s)}} &= \sum_{n=0}^{\infty}\left[C_{2n}I_n(\bar{k}_{2s}r) + D_{2n}K_n(\bar{k}_{2s}r)\right]\sin n\theta
\end{aligned} \tag{11}$$

where A_{2n}, B_{2n}, C_{2n} and D_{2n} denote unknown complex coefficients, determined by boundary conditions.

Therefore, the total frequency-domain wave fields in the rock mass are represented by $\overline{\phi_1} = \overline{\phi^{(i)}} + \overline{\phi_1^{(s)}}$ and $\overline{\psi_1} = \overline{\psi_1^{(s)}}$, respectively. Similarly, the overall wave fields of liner in the Laplace domain are expressed as $\overline{\phi_2} = \overline{\phi_2^{(s)}}$ and $\overline{\psi_2} = \overline{\psi_2^{(s)}}$, respectively. According to the relationship between the frequency-domain potentials and stress and displacement components, the corresponding displacement and stress components are evaluated by

$$\begin{cases}
\overline{\sigma_{rr}} = \lambda_l\nabla^2\overline{\phi_l} + 2\mu_l\left[\dfrac{\partial^2\overline{\phi_l}}{\partial r^2} + \dfrac{\partial}{\partial r}\left(\dfrac{1}{r}\dfrac{\partial\overline{\psi_l}}{\partial\theta}\right)\right] \\
\overline{\sigma_{\theta\theta}} = \lambda_l\nabla^2\overline{\phi_l} + 2\mu_l\left[\dfrac{1}{r}\left(\dfrac{\partial\overline{\phi_l}}{\partial r} + \dfrac{1}{r}\dfrac{\partial^2\overline{\phi_l}}{\partial\theta^2}\right) + \dfrac{1}{r}\left(\dfrac{1}{r}\dfrac{\partial\overline{\psi_l}}{\partial\theta} - \dfrac{\partial^2\overline{\psi_l}}{\partial r\partial\theta}\right)\right] \\
\overline{\sigma_{r\theta}} = \mu_l\left[2\left(\dfrac{1}{r}\dfrac{\partial^2\overline{\phi_l}}{\partial r\partial\theta} - \dfrac{1}{r^2}\dfrac{\partial\overline{\phi_l}}{\partial\theta}\right) + \left(\dfrac{1}{r^2}\dfrac{\partial^2\overline{\psi_l}}{\partial\theta^2} - r\dfrac{\partial}{\partial r}\left(\dfrac{1}{r}\dfrac{\partial\overline{\psi_l}}{\partial r}\right)\right)\right]
\end{cases} \tag{12}$$

$$\begin{cases}
\overline{u_r} = \dfrac{\partial\overline{\phi_l}}{\partial r} + \dfrac{1}{r}\dfrac{\partial\overline{\psi_l}}{\partial\theta} \\
\overline{u_\theta} = \dfrac{1}{r}\dfrac{\partial\overline{\phi_l}}{\partial\theta} - \dfrac{\partial\overline{\psi_l}}{\partial r}
\end{cases} \tag{13}$$

Substituting the displacement potentials $\overline{\phi_1}$ and $\overline{\psi_1}$ into Eqs.(13) and (14) results in the frequency-domain stress and displacement components in the rock mass

$$\begin{aligned}
\overline{\sigma_{rr}} = \frac{2\mu_1}{r^2}\sum_{n=0}^{\infty}&\left[e^{-\bar{k}_{1p}d}\varepsilon_n(-1)^n\overline{f_1}(s)\varepsilon_{11}^1(\bar{k}_{1p}r) + A_{1n}\varepsilon_{11}^3(\bar{k}_{1p}r)\right. \\
&\left. + B_{1n}\varepsilon_{12}^3(\bar{k}_{1s}r)\right]\cos n\theta
\end{aligned} \tag{14}$$

$$\begin{aligned}
\overline{\sigma_{r\theta}} = \frac{2\mu_1}{r^2}\sum_{n=0}^{\infty}&\left[e^{-\bar{k}_{1p}d}\varepsilon_n(-1)^n\overline{f_1}(s)\varepsilon_{41}^1(\bar{k}_{1p}r) + A_{1n}\varepsilon_{41}^3(\bar{k}_{1p}r)\right. \\
&\left. + B_{1n}\varepsilon_{42}^3(\bar{k}_{1s}r)\right]\sin n\theta
\end{aligned} \tag{15}$$

$$\begin{aligned}
\overline{\sigma_{\theta\theta}} = \frac{2\mu_1}{r^2}\sum_{n=0}^{\infty}&\left[e^{-\bar{k}_{1p}d}\varepsilon_n(-1)^n\overline{f_1}(s)\varepsilon_{21}^1(\bar{k}_{1p}r) + A_{1n}\varepsilon_{21}^3(\bar{k}_{1p}r)\right. \\
&\left. + B_{1n}\varepsilon_{22}^3(\bar{k}_{1s}r)\right]\cos n\theta
\end{aligned} \tag{16}$$

$$\begin{aligned}
\overline{u_r} = \frac{1}{r}\sum_{n=0}^{\infty}&\left[e^{-\bar{k}_{1p}d}\varepsilon_n(-1)^n\overline{f_1}(s)\varepsilon_{71}^1(\bar{k}_{1p}r) + A_{1n}\varepsilon_{71}^3(\bar{k}_{1p}r)\right. \\
&\left. + B_{1n}\varepsilon_{72}^3(\bar{k}_{1s}r)\right]\cos n\theta
\end{aligned} \tag{17}$$

$$\begin{aligned}
\overline{u_\theta} = \frac{1}{r}\sum_{n=0}^{\infty}&\left[e^{-\bar{k}_{1p}d}\varepsilon_n(-1)^n\overline{f_1}(s)\varepsilon_{81}^1(\bar{k}_{1p}r) + A_{1n}\varepsilon_{81}^3(\bar{k}_{1p}r)\right. \\
&\left. + B_{1n}\varepsilon_{82}^3(\bar{k}_{1s}r)\right]\sin n\theta
\end{aligned} \tag{18}$$

where the detailed expressions of $\varepsilon_{ij}^k(\bullet)$ $(i = 1,\ 2,\ 4,\ 7,\ 8;\ j = 1,\ 2;\ k = 1,\ 3)$ are given in Appendix A. Similarly, substituting the displacement potentials $\overline{\phi_2}$ and $\overline{\psi_2}$ into Eqs.(13) and (14) leads to following frequency-domain stress and displacement components in the liner

$$\begin{aligned}
\overline{\sigma_{rr}} = \frac{2\mu_2}{r^2}\sum_{n=0}^{\infty}&\left[A_{2n}\varepsilon_{11}^4(\bar{k}_{2p}r) + B_{2n}\varepsilon_{11}^3(\bar{k}_{2p}r) + C_{2n}\varepsilon_{12}^4(\bar{k}_{2s}r)\right. \\
&\left. + D_{2n}\varepsilon_{12}^3(\bar{k}_{2s}r)\right]\cos n\theta
\end{aligned} \tag{19}$$

$$\begin{aligned}
\overline{\sigma_{r\theta}} = \frac{2\mu_2}{r^2}\sum_{n=0}^{\infty}&\left[A_{2n}\varepsilon_{41}^4(\bar{k}_{2p}r) + B_{2n}\varepsilon_{41}^3(\bar{k}_{2p}r) + C_{2n}\varepsilon_{42}^4(\bar{k}_{2s}r)\right. \\
&\left. + D_{2n}\varepsilon_{42}^3(\bar{k}_{2s}r)\right]\sin n\theta
\end{aligned} \tag{20}$$

$$\begin{aligned}
\overline{\sigma_{\theta\theta}} = \frac{2\mu_2}{r^2}\sum_{n=0}^{\infty}&\left[A_{2n}\varepsilon_{21}^4(\bar{k}_{2p}r) + B_{2n}\varepsilon_{21}^3(\bar{k}_{2p}r) + C_{2n}\varepsilon_{22}^4(\bar{k}_{2s}r)\right. \\
&\left. + D_{2n}\varepsilon_{22}^3(\bar{k}_{2s}r)\right]\cos n\theta
\end{aligned} \tag{21}$$

$$\begin{aligned}
\overline{u_r} = \frac{1}{r}\sum_{n=0}^{\infty}&\left[A_{2n}\varepsilon_{71}^4(\bar{k}_{2p}r) + B_{2n}\varepsilon_{71}^3(\bar{k}_{2p}r) + C_{2n}\varepsilon_{72}^4(\bar{k}_{2s}r)\right. \\
&\left. + D_{2n}\varepsilon_{72}^3(\bar{k}_{2s}r)\right]\cos n\theta
\end{aligned} \tag{22}$$

$$\begin{aligned}
\overline{u_\theta} = \frac{1}{r}\sum_{n=0}^{\infty}&\left[A_{2n}\varepsilon_{81}^4(\bar{k}_{2p}r) + B_{2n}\varepsilon_{81}^3(\bar{k}_{2p}r) + C_{2n}\varepsilon_{82}^4(\bar{k}_{2s}r)\right. \\
&\left. + D_{2n}\varepsilon_{82}^3(\bar{k}_{2s}r)\right]\sin n\theta
\end{aligned} \tag{23}$$

where the expressions of $\varepsilon_{ij}^k(\bullet)$ $(i = 1,\ 2,\ 4,\ 7,\ 8;\ j = 1,\ 2;\ k = 3,\ 4)$ in detail are represented by Appendix A. Based on the differential relation in the Laplace domain, the frequency-domain velocity components in the rock mass or the liner are represented by $\overline{v_r} = s\overline{u_r}$ and $\overline{v_\theta} = s\overline{u_\theta}$.

2.3. Frequency-domain solutions of wave equations in fluid

The lined tunnel is filled with the no-viscous compressible ideal fluid and the equation of motion for an inviscid fluid that cannot support shear traction is expressed as

$$K_w\nabla\nabla\boldsymbol{u}_w = \rho_w\frac{\partial^2\boldsymbol{u}_w}{\partial t^2} \tag{24}$$

where $\boldsymbol{u}_w$ denotes the displacement in the inviscid fluid. Based on the Helmholtz decomposition principle, displacement vector is represented by $\boldsymbol{u}_w = \nabla\phi_w^{(s)}$. Substituting the potential into Eq.(24) leads to the following time-domain wave equation.

$$K_w\nabla^2\phi_w^{(s)} = \rho_w\frac{\partial^2\boldsymbol{u}_w}{\partial t^2} \tag{25}$$

Applying the Laplace transform to Eq.(25) results in the following frequency-domain equation.

$$K_w\nabla^2\overline{\phi_w^{(s)}} = \rho_w s^2\overline{\phi_w^{(s)}} \tag{26}$$

The general solution of Eq.(26) in the Laplace domain is given by

$$\overline{\phi_w^{(s)}} = \sum_{n=0}^{\infty}A_{3n}I_n(\bar{k}_{3p}r)\cos n\theta \tag{27}$$

where A_{3n} denotes the undetermined coefficient, obtained by the boundary conditions. $\bar{k}_{3p} = s/C_w$ with $C_w = \sqrt{K_w/\rho_w}$ represents the longitudinal wavenumber in the inviscid medium. In the ideal fluid, the displacement and pressure components are expressed as

Table1
The Iseger algorithm parameters.

λ_j	β_j
0.00000000	1.00000000
6.28318530	1.00000000
12.5663706	1.00000015
18.8502914	1.00081841
25.2872172	1.09580332
34.2969716	2.00687652
56.1725527	5.94277512
170.533131	54.9537264

$$\begin{aligned}
\overline{u_r} &= \frac{\partial \overline{\phi_w^{(s)}}}{\partial r} = \frac{1}{r}\sum_{n=0}^{\infty}\left[A_{3n}\varepsilon_{71}^{4}\left(\overline{k}_{3p}r\right)\right]\cos n\theta \\
\overline{u_\theta} &= \frac{1}{r}\frac{\partial \overline{\phi_w^{(s)}}}{\partial \theta} = \frac{1}{r}\sum_{n=0}^{\infty}\left[A_{3n}\varepsilon_{81}^{4}\left(\overline{k}_{3p}r\right)\right]\sin n\theta \\
\overline{\sigma_{rr}} = \overline{\sigma_{\theta\theta}} &= k_w\nabla^2\overline{\phi_w^{(s)}} = \frac{2\mu_2}{r^2}\sum_{n=0}^{\infty}\left[A_{3n}\overline{k}_{2s}^{2}r^2\rho_w/(2\rho_2)I_n\left(\overline{k}_{3p}r\right)\right]\cos n\theta
\end{aligned} \tag{28}$$

where the expressions of $\varepsilon_{ij}^{k}(\bullet)$ in detail are given in Appendix A.

2.4. Boundary conditions and normalization

In engineering practice, an imperfect interface frequently exists between the rock mass and the lining due to surface irregularities, waterproof board, microcracks, foliation, meso-scale cavities, joints, faults or wall roughness [7,8,10], which prevents full contact. In the existing investigations [7,9,10,40], the spring model is employed to model and present the mechanical characteristics of the rock mass-liner imperfect interface. The spring model assumes that stress components are characterized by continuity, while the displacement components present discontinuous characteristics, where the radial and shear tractions are proportional to the corresponding displacement jumps [11]. Based on the concept mentioned above, the boundary conditions at the rock mass-liner interface ($r = b$) are represented by

$$\begin{aligned}
&\overline{\sigma_{bb,R}} = \overline{\sigma_{bb,L}}, \quad \overline{\sigma_{b\theta,R}} = \overline{\sigma_{b\theta,L}} \\
&\overline{\sigma_{bb,R}} = K_r\left(\overline{u_{b,R}} - \overline{u_{b,L}}\right), \quad \overline{\sigma_{b\theta,R}} = K_\theta\left(\overline{u_{\theta,R}} - \overline{u_{\theta,L}}\right)
\end{aligned} \tag{29}$$

where $\overline{\sigma_{bb,R}}$, $\overline{\sigma_{bb,L}}$, $\overline{\sigma_{b\theta,R}}$, $\overline{\sigma_{b\theta,L}}$, $\overline{u_{b,R}}$, $\overline{u_{b,L}}$, $\overline{u_{\theta,R}}$ and $\overline{u_{\theta,L}}$ respectively stand for the stress and displacement components, where the subscripts R and L represent the corresponding components in the rock mass and liner.

At the inner boundary of the lined tunnel ($r = a$), the radial displacement and stress present continuous characteristics, while the shear traction vanishes, leading to the following equations.

$$\begin{aligned}
&\overline{\sigma_{aa,L}} = \overline{\sigma_{aa,w}} \\
&\overline{u_{a,L}} = \overline{u_{a,w}} \\
&\overline{\sigma_{a\theta,L}} = 0
\end{aligned} \tag{30}$$

where the subscript w denotes stress or displacement components in water.

Combining Eqs.(14) -(23) with Eqs.(28)-(30), the following matrix equation in the frequency domain is determined for any order n.

$$\boldsymbol{R}_{7\times7}\boldsymbol{Q}_{7\times1} = e^{-\overline{k}_{1p}d}\overline{f_1}(s)\varepsilon_n(-1)^n\boldsymbol{P}_{7\times1} \tag{31}$$

where the detailed element expressions of the coefficient matrix $\boldsymbol{R}_{7\times7}$ are provided in Appendix B. The vectors $\boldsymbol{Q}_{7\times1}$ and $\boldsymbol{P}_{7\times1}$ are represented by

$$\boldsymbol{Q}_{7\times1} = \left[A_{1n}, B_{1n}, A_{2n}, B_{2n}, C_{2n}, D_{2n}, A_{3n}\right]^T \tag{32}$$

$$\boldsymbol{P}_{7\times1} = \left[\overline{\mu}E_{11}^{(1)}\left(\overline{k}_{1p}b\right), \overline{\mu}E_{41}^{(1)}\left(\overline{k}_{1p}b\right), E_{71}^{(1)}\left(\overline{k}_{1p}b\right) - \frac{2\mu_1}{bk_r}E_{11}^{(1)}\left(\overline{k}_{1p}b\right), E_{81}^{(1)}\left(\overline{k}_{1p}b\right) - \frac{2\mu_1}{bk_\theta}E_{41}^{(1)}\left(\overline{k}_{1p}b\right), 0, 0, 0\right]^T \tag{33}$$

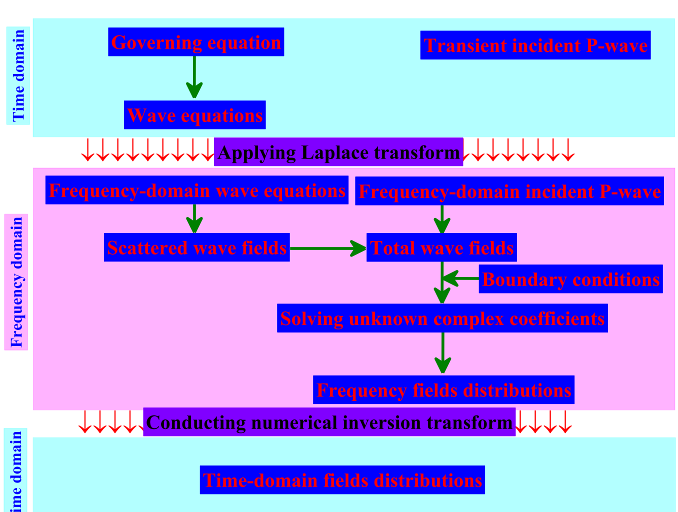

Fig. 2. Computational flowchart of theoretical time-domain response.

where $E_{ij}^{k}(\bullet)$ denote the value of $\varepsilon_{ij}^{k}(\bullet)$ at the rock mass-liner or liner-fluid interface. $\overline{\mu} = \mu_1/\mu_2$ represents the ratio of shear modulus of the rock mass to that of the liner.

When the harmonic incident P-wave propagates through the intact homogeneous rock mass, the frequency-domain stress intensity and peak velocity in the propagation direction are represented by $\overline{\sigma_0} = \mu_1\overline{k}_{1s}^2$ and $\overline{v_0} = s^2/C_{1p}$, respectively, which are regarded as the normalization factors [6]. Therefore, the dynamic stress concentration factors and velocity scaling factors in the Laplace domain are defined as [27,28]

$$\begin{aligned}
&\overline{\sigma_{rr}}(s) = \overline{\sigma_{rr}}/\overline{\sigma_0} \\
&\overline{\sigma_{\theta\theta}}(s) = \overline{\sigma_{\theta\theta}}/\overline{\sigma_0} \\
&\overline{\sigma_{r\theta}}(s) = \overline{\sigma_{r\theta}}/\overline{\sigma_0}
\end{aligned} \tag{34}$$

$$\begin{aligned}
&\overline{v_r}(s) = \overline{v_r}/\overline{v_0} \\
&\overline{v_\theta}(s) = \overline{v_\theta}/\overline{v_0}
\end{aligned} \tag{35}$$

where $\overline{\sigma_{rr}}(s)$, $\overline{\sigma_{\theta\theta}}(s)$, $\overline{\sigma_{r\theta}}(s)$, $\overline{v_r}(s)$ and $\overline{v_\theta}(s)$ represent the non-dimensional stress and velocity responses in the frequency domain. Using numerical inversion algorithm represented by Section 2.5, the frequency-domain response mentioned above can be inverted into the corresponding time-domain solution.

2.5. Numerical inversion algorithm

The numerical inversion algorithms including combination of Gave functionals, deformation of the Bromwich contour, Fourier series expansion and Laguerre function expansion are frequently employed to invert the frequency-domain response into the corresponding time-domain counterpart [41]. Various algorithms exhibit different computational accuracy and numerical stability. Based on the existing investigations [41–45], the Den Iseger is adopted in this paper. The Den Iseger algorithm is based on the Poisson summation formula, which belongs to the category of Fourier series expansion method. Its core advantage lies in the ability to accurately handle discontinuous, singular and rapidly varying functions.

The algorithm employs Gaussian quadrature and the fast Fourier transform (FFT) to approximate an infinite series and compute time-domain results. Key parameters for this algorithm include the total computation duration $t_{\max}$, the number of sampling points M in the range of $[0,\ t_{\max}]$, the step size $\Delta = t_{\max}/(M-1)$, the oversampling factor $n_D rp$ (original proposal recommendation nrp=8 and $M_2 = n_D rpM$), and the function-type parameter n_D. For stable and reliable inversion, two fundamental conditions must be satisfied: The number of sampling points must satisfy $M > 10t_{\max}$ and the inversion of the step size, $1/\Delta$, must be an integer. The Den Iseger algorithm includes the following steps. First, the real parts of the frequency-domain functions at discrete points are evaluated by

$$\overline{h}_{jk_1} = \mathrm{Re}\left\{\overline{h}\left(\frac{a_D + \lambda_j i + \frac{2\pi i k_1}{M_2}}{\Delta}\right)\right\}, \overline{h}_{k_1} = \frac{4}{\Delta}\sum_{j=1}^{n_D/2}\beta_j\{\overline{h}_{jk_1}\} \tag{36}$$

$$\overline{h}_0 = \frac{1}{2}\sum_{j=1}^{\frac{n_D}{2}}\beta_j(\overline{h}_{j0} + \overline{h}_{jM_2}) \tag{37}$$

where $M_2 = 8M$, $a_D = 44/M_2$, $n_D = 16$, k_1 ranges from zero to M_2 and j ranges from one to $n_D/2$.

According to the reference [43], the algorithm parameters of the numerical inversion are selected as Table 1.

Moreover, when k_1 ranges from zero to $M_2 - 1$, substituting Eqs.(36) and (37) into Eq.(38) evaluates the following real numbers using the backwards FFT algorithm.

$$h_{m_1} = \frac{1}{M_2}\sum_{k_1=0}^{M_2-1}\overline{h}_{k_1}\cos\left(\frac{2\pi m_1 k_1}{M_2}\right) \tag{38}$$

Finally, when m_1 ranges from zero to $M-1$, the ultimate time-domain solutions inverted by the numerical algorithm on a regular grid of time points are evaluated by

$$h(t) = e^{a_D m_1} h_{m_1} \tag{39}$$

Based on aforementioned descriptions, the overall computational flowchart for a lined diversion tunnel subjected to blasting or earthquake load in a full space is illustrated in Fig. 2.

3. Computational accuracy analysis and verification

3.1. Error analysis

The theoretical derivation process in Section 2 reveals that the precision of the ultimate time-domain solutions is affected by the inversion algorithm and the truncation term of the infinite series. The existing investigations regarding transient unloading of in-situ stress in deep engineering and dynamic perturbation in half or full space have revealed that the Den Iseger algorithm presents high computational accuracy and excellent numerical stability so that the error originating from the numerical inversion is ignored [25,26,41–48]. To investigate the error caused by the truncation term of displacement potentials, the following time-domain relative error function of the circumferential stress is defined as $e_r = \left|\frac{\sigma_{\theta\theta}^{(n)}(t) - \sigma_{\theta\theta}^{(n-2)}(t)}{P_e}\right|$ at the inner boundary of the diversion tunnel. When the relative error e_r is less than 10^{-3} in time interval $[0, t_{\max}]$, this summation term is regarded as the final truncation term. Here the physical parameters including elastic modulus, Poisson's ratio and mass density of the rock mass and the liner as well as bulk modulus and mass density of the fluid are 50 GPa, 30 GPa, 0.22, 0.25, 2700 kg/m^3, 2500 kg/m^3, 2.18 GPa and 1000 kg/m^3, respectively. For the case of b= 1.2a, d=b, dimensionless rising time $\tau_r = \frac{C_{1p}t_r}{b} = 2.0$ and total duration $\tau_s = 10$, Fig. 3 depicts the time-history variations regarding the relative function of the right sidewall at the fluid-liner interface. It can be identified that remarkable improvement of the computational precision appears as the truncation term of the infinite series increases. Considering the time complexity and the computational accuracy, the truncation term $n = 16$ is adopted in the following calculation.

3.2. Comparisons of degenerate solutions with the existing results

In this section, it is assumed that the radial and hoop elastic coefficients of the imperfect interface tend to be infinity (K_r=K_θ=1000 μ_1/b) so that the imperfect model is degenerate into the perfect counterpart. When the physical parameters of the liner are consistent with those of the rock mass and the bulk modulus of the fluid tends to be zero, the current computational model is degenerate into the empty cavity presented by Li et al. [22]. When the physical and disturbance parameters including elastic modulus, Poisson's ratio, mass density, dimensionless rising and total times are 18.73 GPa, 0.206, 2750 kg/m^3, 20 and 100, respectively, consistent with the reference [22]. Fig. 4 plots the non-dimensional time-history curves of the circumferential stress at the right sidewall and roof. It is observed that the present degenerate solutions are consistent with the existing results obtained by combining WFEM, Fourier synthesis method and Duhamel integral.

Here the physical parameters including elastic modulus, Poisson's ratio and mass density are 50 GPa, 0.22 and 2700 kg/m^3 for the rock mass and 30 GPa, 0.25 and 2500 kg/m^3 for the liner, respectively, same as the reference [27]. The bulk modulus of the fluid tends to be zero so that the current computational model is degenerate into the single lined tunnel. For the case of K_r= 0.1 μ_1/b, K_θ= 100 μ_1/b, b= 6.5 m, a= 6.0 m, dimensionless rising time τ_r= 5.0 and total duration τ_s= 25, Fig. 5 displays the dimensionless variations of hoop stress of the two sidewalls and roof at the rock mass-liner interface and inner boundary. It is seen that the current degenerate results are in good agreement with the existing solutions in reference [27].

Here the radial and hoop elastic coefficients of the imperfect interface tend to be infinity (K_r=K_θ=100 μ_1/b) so that the imperfect model can be degenerate into the perfect counterpart. The physical parameters of the solids and geometry dimensions of diversion tunnel are consistent with the preceding lined tunnel, while the bulk modulus and mass density of the fluid are set as 2.18 GPa and 1000 kg/m^3, respectively. The dimensionless rising time τ_r= 2.0 and total duration τ_s= 10.0 for triangular disturbance load are adopted. Fig. 6 plots dimensionless hoop stress response at the rock mass-liner interface and fluid pressure response at the tunnel center. It is identified that the current solutions are consistent with those presented by Li et al. [21], which are based on combination of WFEM, Fourier synthesis method and Duhamel integral.

3.3. Comparisons with numerical results

Based on a self-developed software, namely Cellular Automata Software for engineering Rockmass fracturing process (CASRock) including elasto-plastic cellular automaton (EPCA), dynamic elasto-plastic cellular automaton (D-EPCA) [47], viscous elasto-plastic cellular automaton (V-EPCA), thermo-hydro-mechanical-chemical elasto-plastic cellular

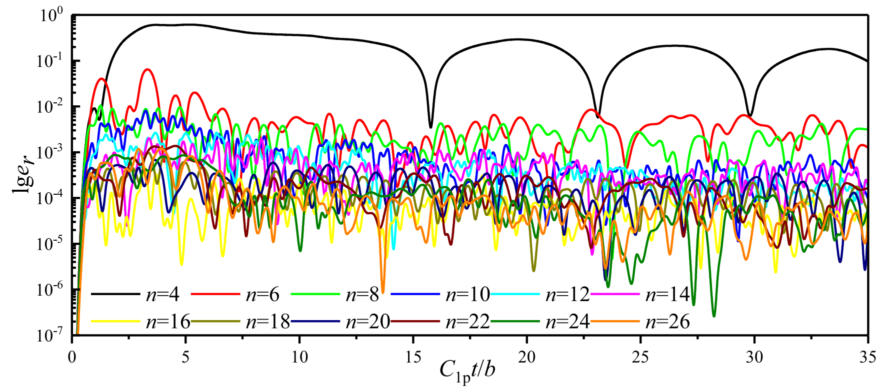

Fig. 3. Relative error curves of right sidewall at the liner-fluid interface under various truncation terms.

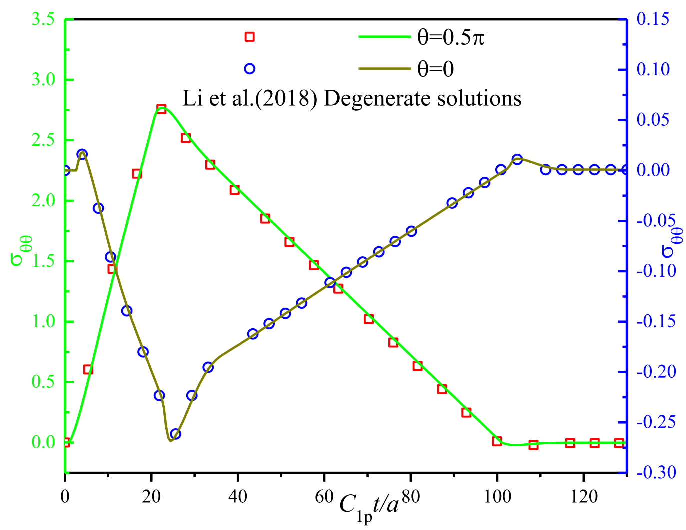

Fig. 4. The dimensionless circumferential stress variations at the right sidewall and roof.

automaton (THMC-EPCA) and rock discontinuous cellular automaton (RDCA), numerical simulation is performed. Here, only D-EPCA is adopted and a numerical model considering effect of water is established to further verify the theoretical results. The numerical model with dimensions 120 m × 120 m is adopted and physical parameters for solids, fluid and geometric parameters are consistent with aforementioned lined diversion tunnel. The left border of the computational model is subjected to triangular blasting P-wave, where the rising and total times are 2.83 and 14.14 ms, respectively. The upper and lower boundaries are subjected to normal constraint and right boundary is set as viscous artificial boundary condition (VABC) to absorb the stress wave. Fig. 7 displays the dimensionless time-domain variation of stress in surrounding rock and liner and fluid pressure at the tunnel center. It is identified that the theoretical solutions at monitoring points are consistent with numerical results obtained by D-EPCA, verifying the proposed method.

4. Transient response induced by blasting P-wave

In this section, the physical and geometric parameters for the rock mass, liner and fluid are consistent with those specified in Section 3.1. Time is initialized when the wavefront of the disturbance P-wave reaches the rock mass-liner interface. The transient P-wave is simplified as a triangular load with peak value P_e, rising time t_r and total duration t_s. The relation between the outer and inner radii is $b=1.2a$. The non-dimensional rising time $\tau_r = 2.0$ and total duration $\tau_s = 10$ are adopted unless otherwise specified.

4.1. Effect of physical parameters of rock mass

For the case of K_θ=K_r= 100 μ_1/b, elastic modulus of the rock mass ranging from 15 to 45 GPa, Fig. 8 depicts the dimensionless

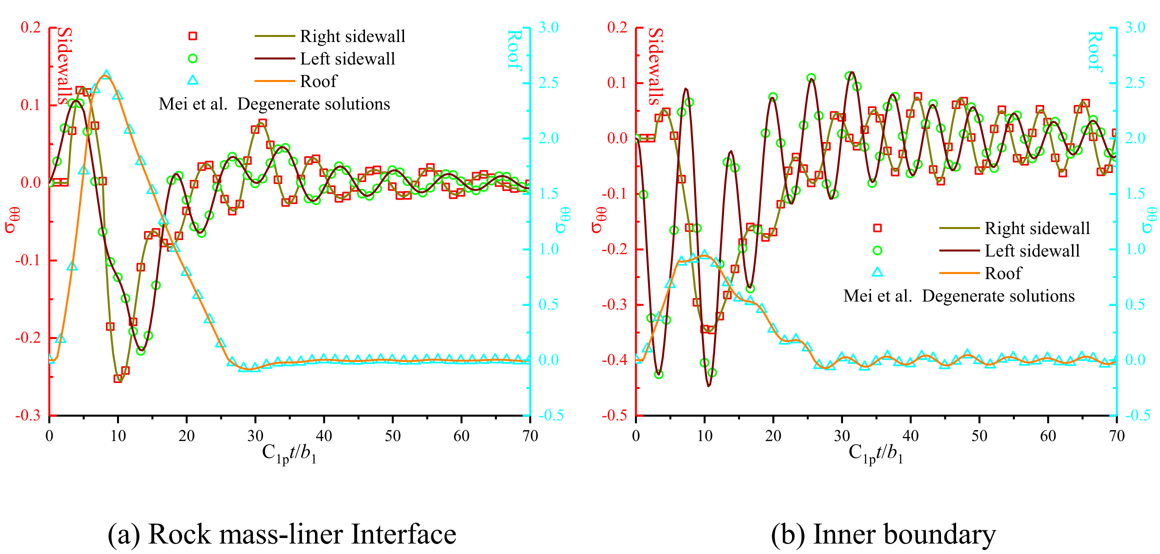

Fig. 5. The dimensionless circumferential stress variations at the rock mass-liner interface and inner boundary.

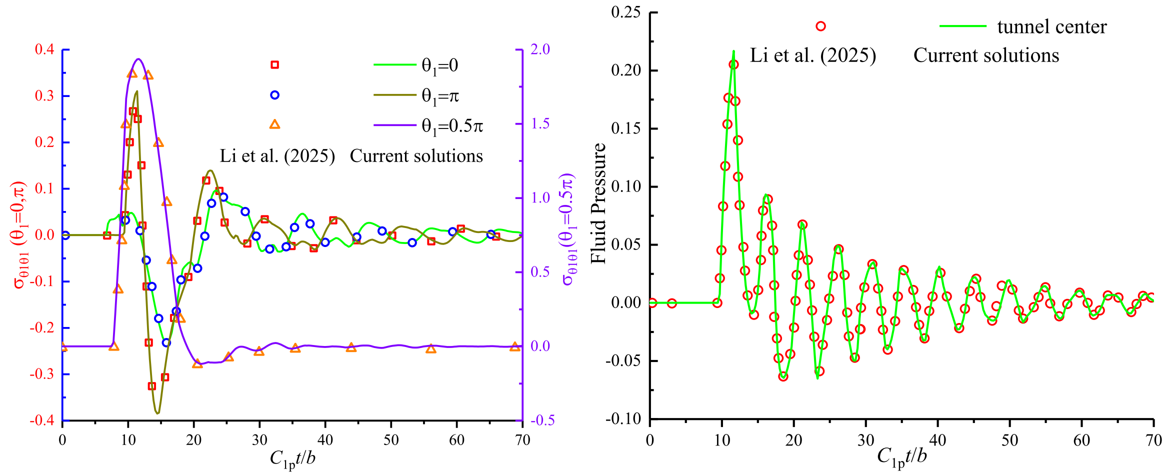

(a) At rock mass-liner interface (b) Tunnel center

Fig. 6. The dimensionless circumferential stress and pressure variations at rock mass-liner interface and tunnel center under triangular P-wave.

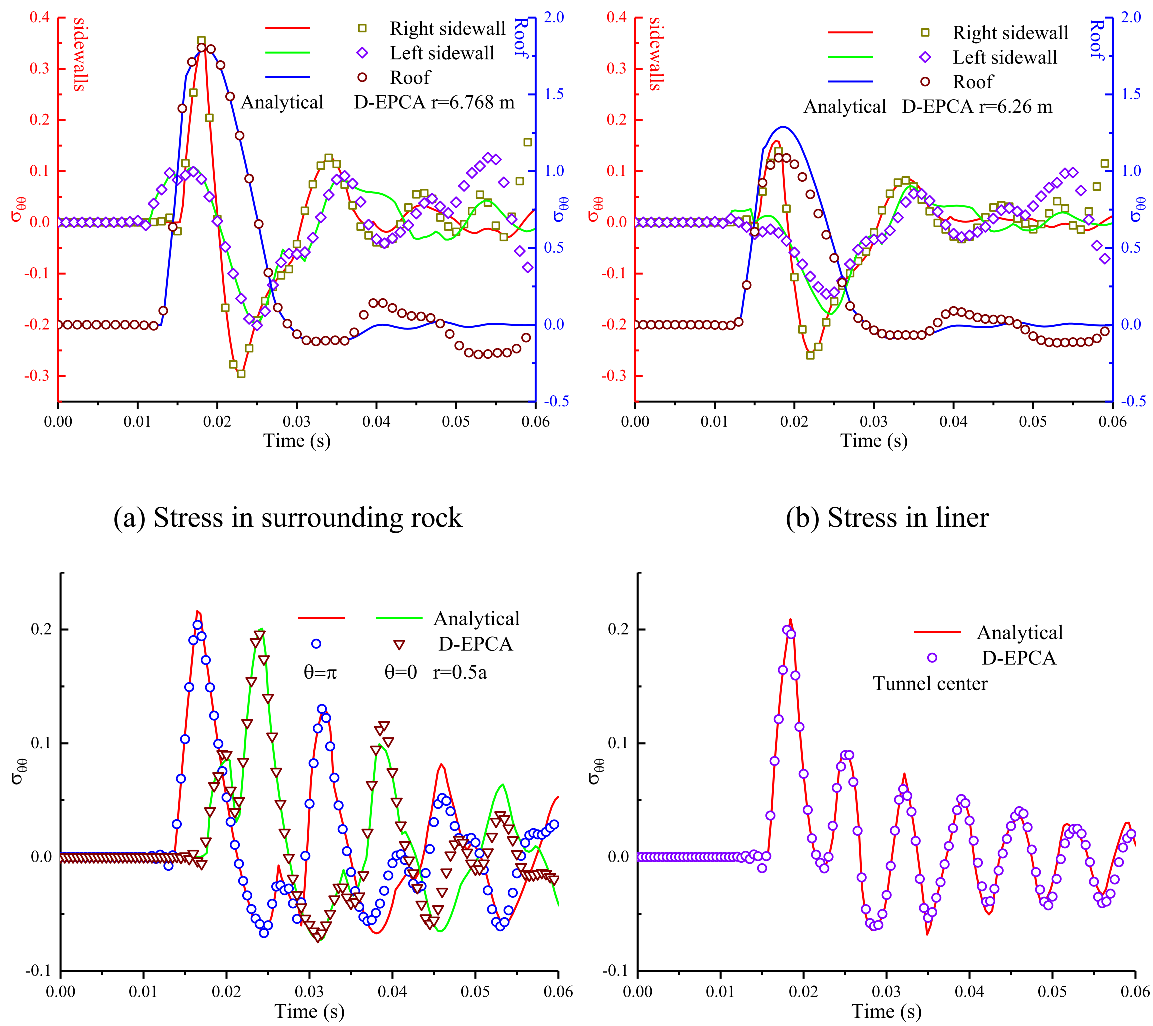

(a) Stress in surrounding rock (b) Stress in liner

(c) Fluid pressure at r=0.5a (d) Fluid pressure at tunnel center

Fig. 7. The stress and pressure response around the diversion tunnel subjected to horizontal triangular blasting P-wave.

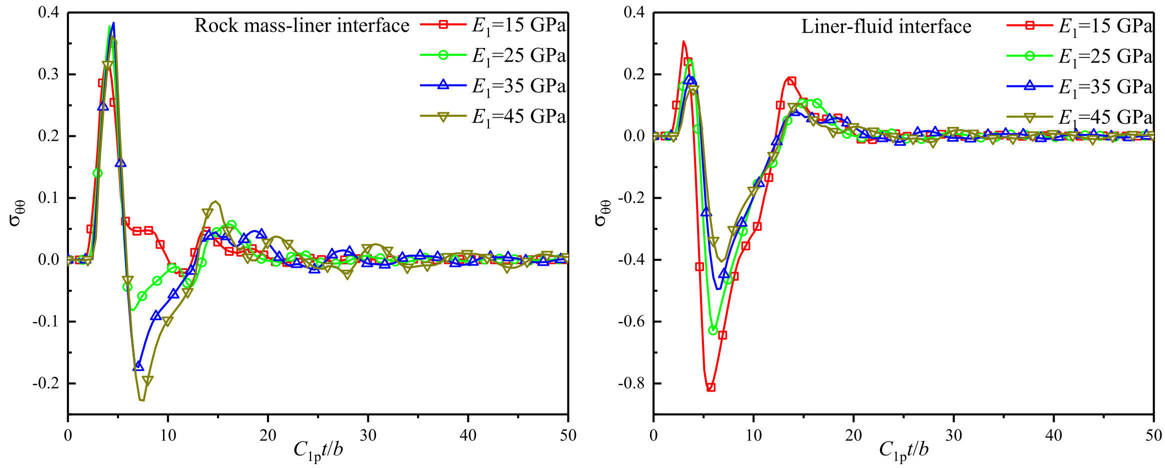

(a) θ=0

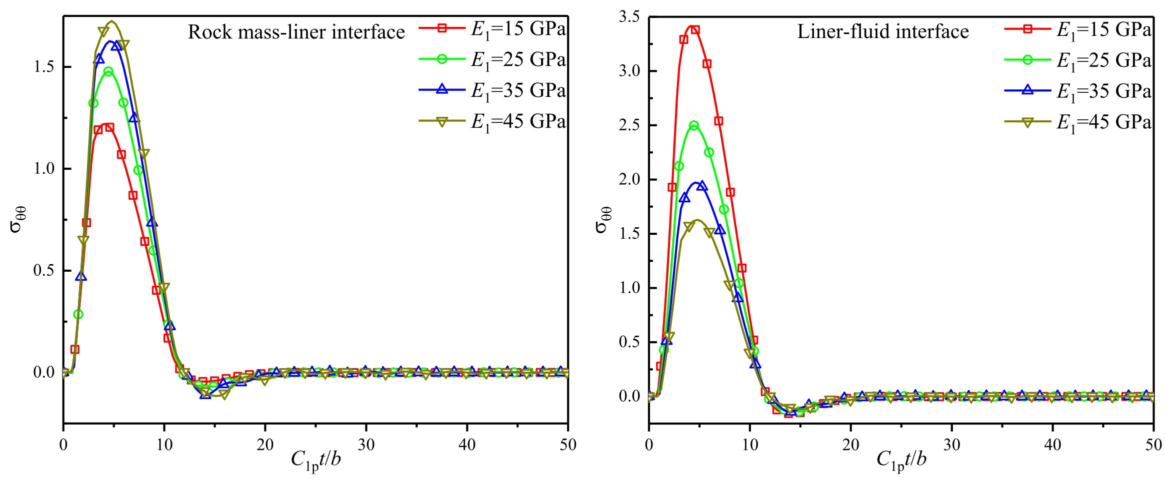

(b) θ=0.5π

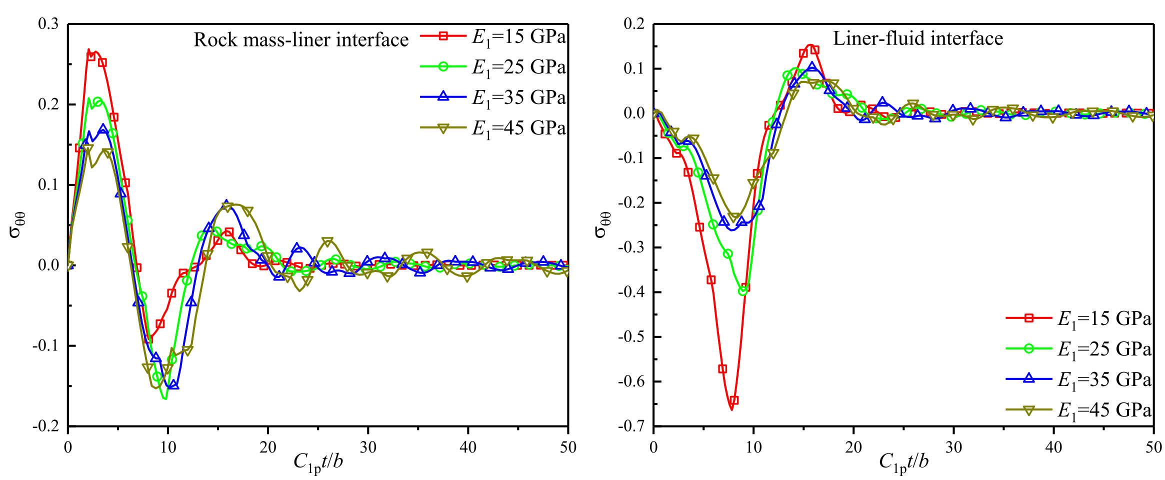

(c) θ=π

Fig. 8. The dimensionless circumferential stress variations at the rock mass-liner and liner-fluid interfaces for different elastic modulus of the rock mass.

circumferential stress variations at the rock mass-liner and liner-fluid interfaces. As illustrated in Fig. 8a, the hoop stress of the shadow sidewall at the rock mass-liner interface first undergoes compressive stress concentration, followed by tensile stress concentration, and finally rebounds to near zero. With an increase of elastic modulus in the rock mass, the peak tensile stress at the rock mass-liner interface gradually increases, while the peak compressive stress first increases and then decreases. A similar trend is observed at the shadow sidewall of the liner-fluid interface, while the peak compressive and tensile stresses both present a decline. As demonstrated in Fig. 8b, the roof of the diversion tunnel is characterized by compressive stress concentration. As the elastic modulus increases, peak stress at the rock mass-liner interface first presents an increase and then stabilizes, while the opposite trend appears at the liner-fluid interface. As depicted in Fig. 8c, the time-history curves of tangential stress at the incident sidewall of the rock mass-liner interface first undergo a transformation from compressive stress concentration to tensile counterpart, then experience reciprocating fluctuations, and finally converge to the undisturbed state. The peak compressive stress at the rock mass-liner interface presents a reduction as the elastic modulus of the rock mass increases, while counterpart of tensile stress first presents an increase and then undergoes a decline. At the incident sidewall of the liner-fluid interface, time-history curves of tangent stress first undergo tensile stress concentration, then rebound, and ultimately stabilize at the undisturbed state, where the peak tensile stress gradually decreases as the elastic modulus of the rock mass increases. Compared with the empty or lined cavity in the references [22,30], the more remarkable oscillations for time-history response appear for the fluid-filled lined tunnel even if the imperfect interface is degenerate into the perfect counterpart.

Fig. 9 displays the dimensionless fluid pressure variations at $r = 0.5a$ and the tunnel center under blasting P-wave. It is identified that the pronounced wave impedance variation between solid and fluid induces repeated pressure transmission and forms multiple scattering superposition. This repeated loading and unloading process is directly manifested as pressure fluctuations. As the elastic modulus of the rock mass increases, peak fluid pressure gradually decreases and oscillations of time-history curves gradually intensify. Compared with the response in the rock mass and the liner, time-history fluctuations in the fluid are more remarkable.

4.2. Effect of radial elastic coefficient

For the case of $K_\theta = 100\mu_1/b$, $K_r = 0.1\mu_1/b$, μ_1/b, $10\mu_1/b$ and $100\mu_1/b$, Fig. 10 displays the time-history variations of dimensionless circumferential stress at the two sidewalls and roof of the rock mass-liner and liner-fluid interfaces. It is identified that reciprocating compressive-tensile stress alternations with a gradual decreasing amplitude appear at the two sidewalls for the small K_r (e.g. $K_r = 0.1\mu_1/b$). As K_r increases, the maximum tensile-compressive stress amplitude gradually decreases and the time-history oscillations induced by the repeated stress accumulation and release also gradually weaken at the two sidewalls. As demonstrated in Fig. 10b, the roof also undergoes remarkable oscillations for the small K_r. The peak compressive stress around the rock mass-liner interface first presents a gentle reduction and then maintains a stable constant as the K_r increases, while counterpart around the liner-fluid interface presents a gradual increase and then maintains a stable value. When the K_r exceeds $10\mu_1/b$, the dynamic response of the imperfect interface model converges to those of the perfect counterpart.

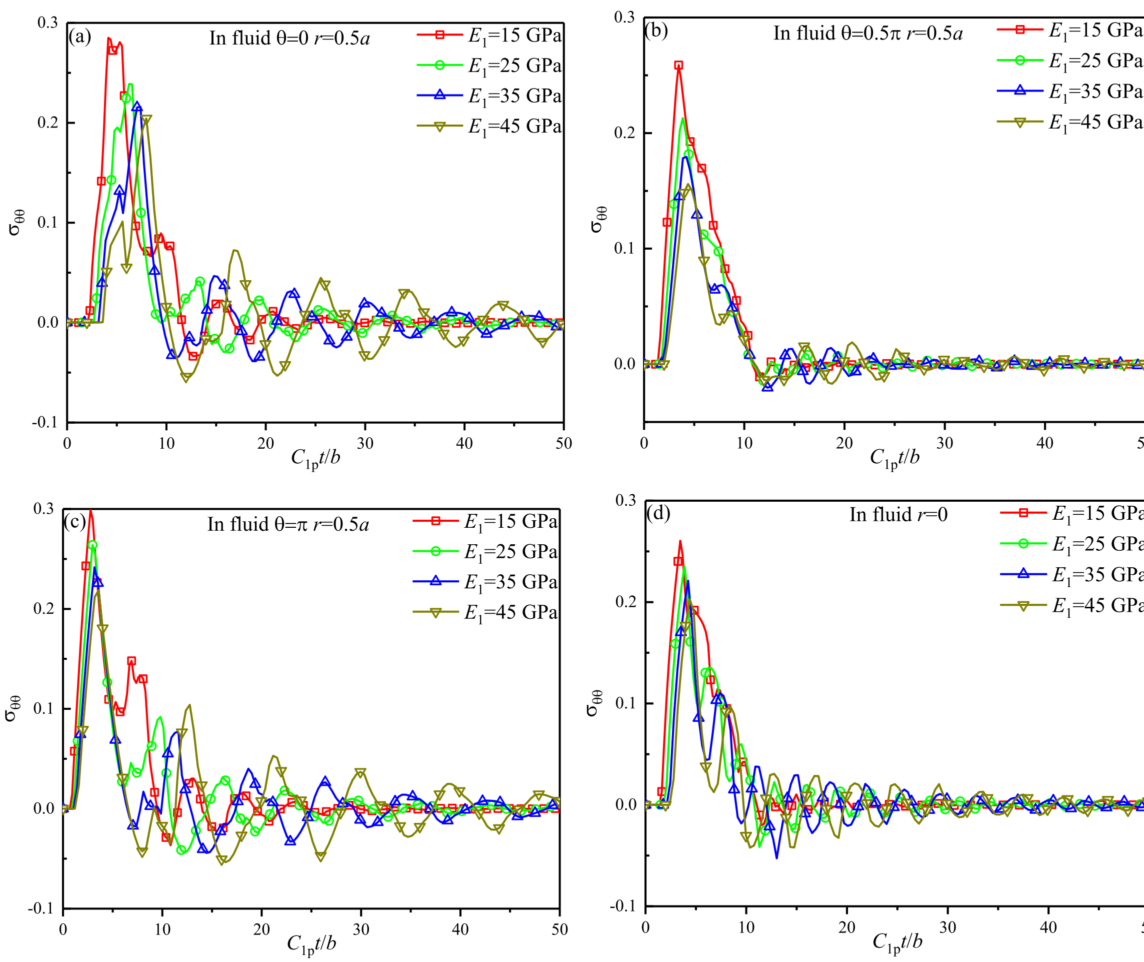

Fig. 9. The dimensionless hoop stress variations in the fluid for different elastic modulus of the rock mass.

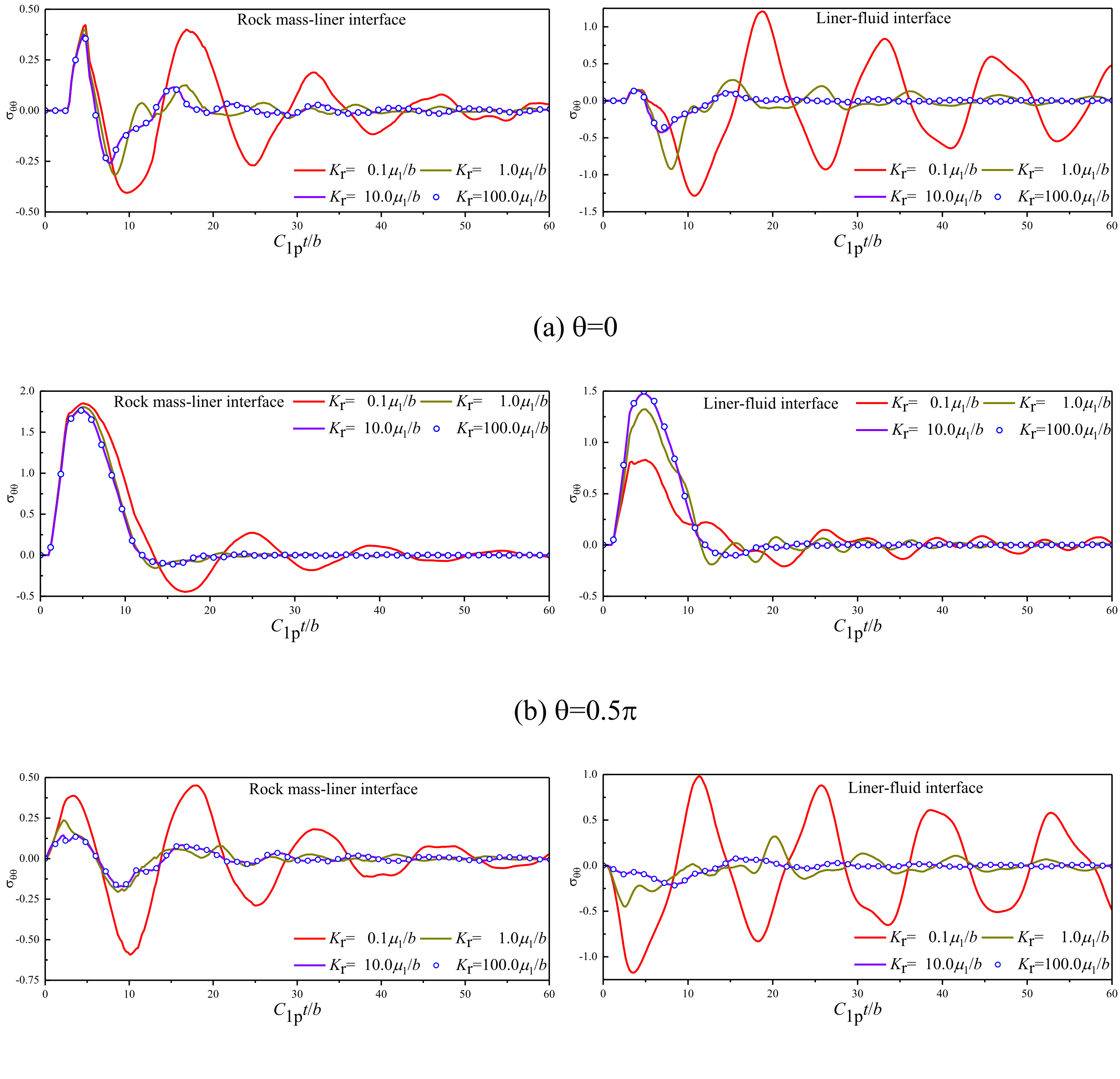

Fig. 10. The dimensionless circumferential stress variations at the rock mass-liner and liner-fluid interfaces under various K_r.

Fig. 11 plots the time histories of fluid pressure at $r = 0.5a$ and the tunnel center when the radial elastic coefficient ranges from $0.1\mu_1/b$ to $100\mu_1/b$. Stronger radial rock mass-liner contact amplifies the amplitude of scattered waves in the liner, resulting in a remarkable fluid pressure amplitude with minimal time-dependent oscillations. In contrast, poor radial contact induces the opposite variation due to the repeated energy accumulation and release. Compared with the dynamic response in the solid domains, the peak dynamic fluid pressure is smaller and exhibits remarkable fluctuations. This discrepancy arises because the solid exhibits higher stiffness and better energy transmission continuity, whereas the fluid is more susceptible to wave dispersion and interface-induced energy scattering, leading to differences in peak magnitude and fluctuation characteristics.

Fig. 12 plots the peak absolute variation of hoop stress at the rock mass-liner and liner-fluid interfaces under blasting P-wave. It can be identified from Fig. 12a that the peak hoop stress at rock mass-liner interface first presents a reduction and then maintains stable distribution as K_r increases. As depicted in Fig. 12b, the peak dynamic hoop stress at the roof first exhibits an increase and then maintains stable value as K_r increases. However, the peak dynamic hoop stress at the two sidewalls generates a reduction and then converges to that of perfect interface model. This variation is consistent with the lined tunnel without fluid filling, while the existence of fluid results in a reduction of compressive stress at the roof and an increase of tensile stress at the two sidewalls.

Fig. 13 plots the temporal and spatial evolutional process of third principal pressure around the diversion tunnel. Due to the various wave impedance among several media, scattering and diffraction appear when wave front reaches around the diversion tunnel, leading to remarkable local dynamic stress concentration. As the elastic modulus of

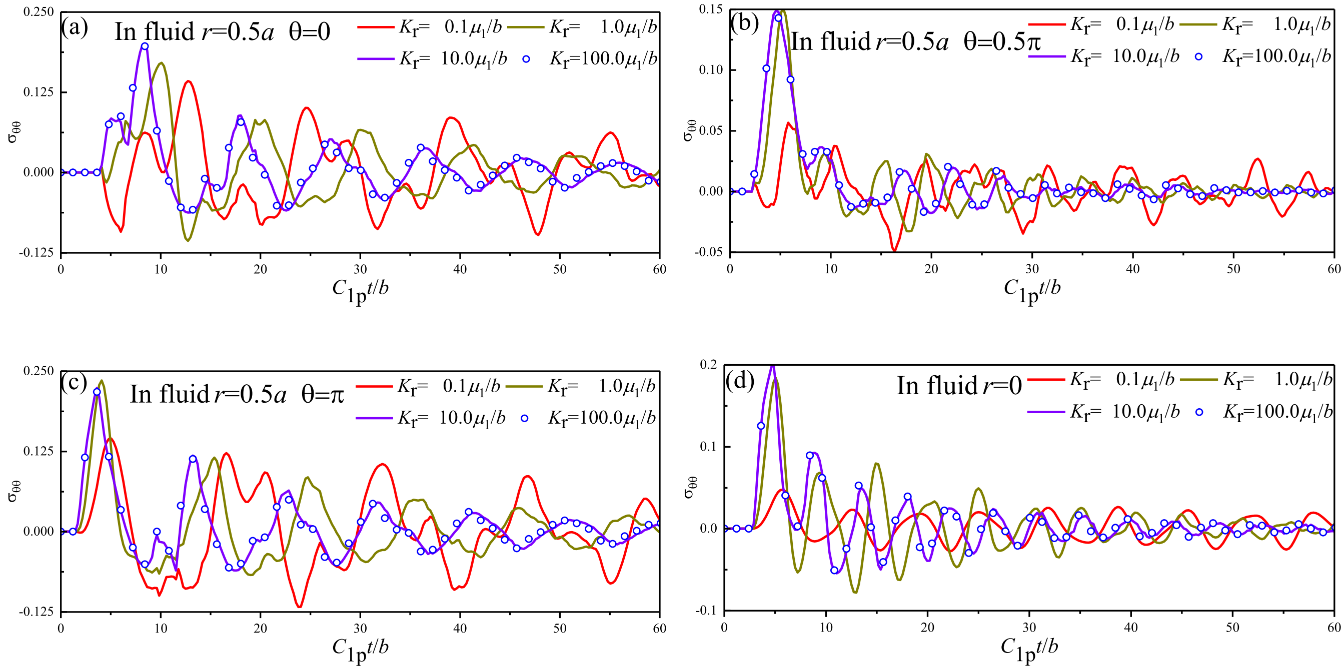

Fig. 11. The dimensionless fluid pressure response under various K_r.

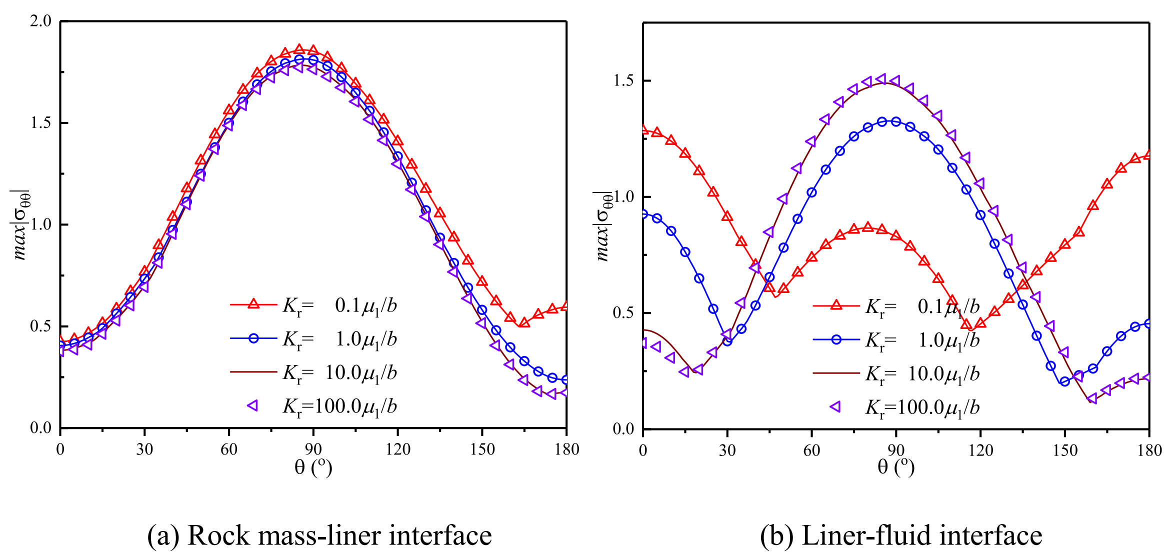

Fig. 12. Distributions of hoop stress at the rock mass-liner and liner-fluid interfaces under various K_r.

rock mass exceeds that of the liner, the stress concentration degree in the rock mass is more pronounced than those of liner and fluid. As time ranges from 13 to 17 ms, stress concentration in rock mass shifts from the left spandrel and corner to the roof and floor. The smaller K_r is, the more remarkable stress concentration degree occurs. Moreover, a discontinuous stress area between the rock mass and the liner appears around the right sidewall. The smaller K_r is, the more pronounced variation occurs.

4.3. Effect of hoop elastic coefficient

For the case of $K_r = 100\mu_1/b$, $K_\theta = 0.1\mu_1/b$, μ_1/b, $10\mu_1/b$ and $100\mu_1/b$, Fig. 14 plots the circumferential stress variations at the sidewalls and the roof. As depicted in Fig. 14a, the right sidewall at the rock mass-liner interface first undergoes low-amplitude compressive stress concentration, followed by tensile stress concentration and ultimately converges to zero. As K_θ increases, the peak tensile stress at the rock mass-liner interface gradually decreases and eventually stabilizes at a stable value. At the liner-fluid interface, a transformation from compressive stress concentration to tensile counterpart occurs and stress fluctuation gradually decreases as K_θ increases. As demonstrated in Fig. 14b, the roof around the rock mass-liner interface is characterized by the compressive stress concentration, where peak value gradually decreases to that of the perfect interface model as K_θ increases. Peak compressive stress at the roof of liner-fluid interface gradually increases and finally maintains a constant as K_θ increases. As illustrated in Fig. 14c, the peak tensile stress at the rock mass-liner interface gradually decreases and then maintains stable constant with increasing K_θ. Stress at the liner-fluid interface generates pronounced oscillations for small K_θ, where a transformation from the compressive stress concentration to tensile counterpart appears as K_θ increases. Compared with dynamic response under various K_r, the stress fluctuations at the rock mass-liner and liner-

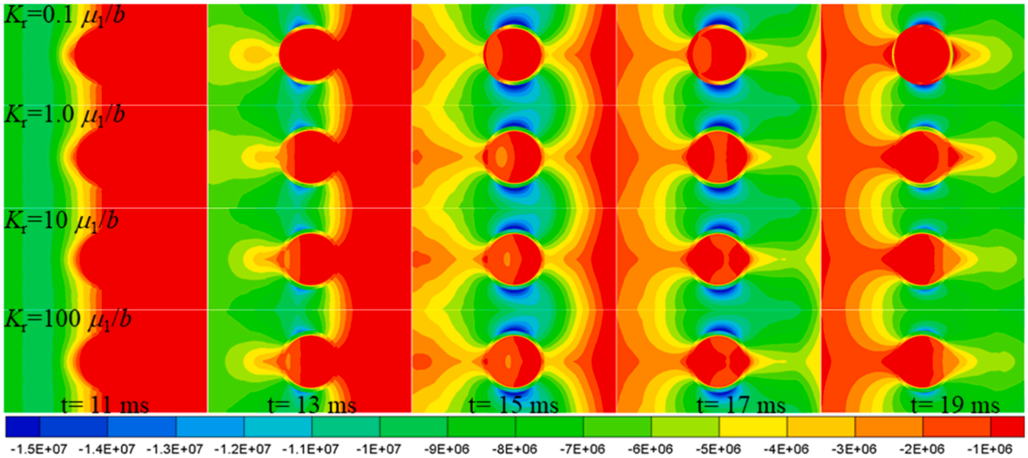

Fig. 13. The evolutional process of the third principal stress around the diversion tunnel under various K_r.

fluid interfaces weaken, revealing that dynamic response of surrounding rock and liner are more sensitive to the variation of K_r.

Fig. 15 plots the time histories of fluid pressure at $r = 0.5a$ and the tunnel center when the hoop elastic coefficient of imperfect interface model ranges from $0.1\mu_1/b$ to $100\mu_1/b$. A consistent temporal evolution pattern is observed for the pressure wave waveforms at all monitoring locations. An initial large-amplitude pressure pulse is followed by reciprocating oscillations with gradually decaying amplitude, which ultimately converge to the undisturbed state. Notably, the fluid pressure variation is immune to K_θ and the time-history response of dynamic pressure remains identical under various K_θ.

K_r characterizes the normal stiffness of the rock mass-liner interface along the radial direction, which serves as the dominant path for stress wave transmission between the solid domains and the fluid, and its variation directly modulates the coupling efficiency of normal stress waves. A high K_r enables rigid, low-loss transmission of radial stress waves to the liner, exciting large-amplitude scattered waves, while a low K_r renders the radial interface compliant, leading to repeated reflection, energy accumulation, and secondary transmission of stress waves at the rock mass-liner gap. K_θ describes the tangential stiffness of the rock mass-liner interface, whose function is limited solely to shear stress transfer and circumferential wave propagation within the solid domains. Fluid pressure is primarily driven by normal stress fluctuations rather than tangential shear effects and variations in K_θ do not affect the transmission efficiency of radial stress waves to the fluid domain. Wide-range adjustments only alter the circumferential distribution of stress inside the liner, rather than exerting a significant influence on the radial liner-fluid coupling process that governs fluid pressure evolution. This fundamental difference in load transmission direction and coupling mechanism is the core reason why fluid pressure response is highly sensitive to K_r yet completely insensitive to K_θ.

Fig. 16 displays the distributions of hoop stress at the rock mass-liner and liner-fluid interfaces under various K_θ. The peak circumferential stress around the roof and two sidewalls of the rock-liner interface presents a gradual reduction and ultimately converges to that of perfect interface model as K_θ increases. In contrast, at the liner-fluid interface, the peak hoop stress around the roof exhibits an increase, while two sidewalls present a reduction and finally converge to that of the perfect interface model.

5. Transient response induced by seismic P-wave

The blasting P-wave is simplified as a triangular curve in Section 4, while this wave simplification fails to capture the actual variation characteristic of seismic P-wave in practical engineering. Herein, a series of continuous piecewise linear functions in Eq.(1) are employed to describe the detailed temporal variation of seismic P-wave, where its acceleration, velocity and displacement time histories are illustrated in Fig. 17. The physical and geometric parameters of rock mass, liner and fluid remain consistent with those presented in Section 3.1 unless otherwise specified.

5.1. Effect of physical parameters of surrounding rock

For the case of K_θ=K_r= 100 μ_1/b (characterized by perfect contact), elastic modulus of the rock mass varied by 15, 25, 35 and 45 GPa, Fig. 18 records the tangential stress time histories at the rock mass-liner and liner-fluid interfaces. As illustrated in Fig. 18a, the peak tensile and compressive stresses at the rock mass-liner interface along the perturbation direction gradually decreases and stress oscillations are gradually attenuated as elastic modulus of rock mass increases. However, the peak tensile and compressive stresses perpendicular to the disturbance direction presents a contrary variation. As plotted in Fig. 18b, the peak tensile and compressive stresses at the liner-fluid interface first presents an increase and then a reduction along the incident direction. Furthermore, along the disturbance direction, the peak stresses at the liner-fluid interface are larger than those at the rock-liner interface. Perpendicular to the incident direction, the stress response at the liner-fluid interface basically maintains consistency, immune to the variation for stiffness of the liner under seismic P-wave. These results indicate that the regions perpendicular to the disturbance direction undergo more pronounced stress variations under seismic P-wave, warranting special attention in practical engineering.

5.2. Effect of radial elastic coefficient

For the case of K_θ= $100\mu_1/b$ and range of K_r from $0.1\mu_1/b$ to $100\mu_1/b$, Fig. 19 displays the time-domain response of radial acceleration at the incident sidewall of both the rock mass-liner and liner-fluid interfaces. It is observed from Fig. 19a that the acceleration variation at the incident sidewall of rock mass-liner interface presents basic consistency, revealing that vibration of acceleration is immune on the rock mass-liner contact state. However, pronounced fluctuations occur around the imperfect rock mass-liner interface. The worse the radial contact, the more remarkable oscillations. As illustrated in Fig. 19b, although the radial contact is characterized by perfect contact (K_r= $100\mu_1/b$), the radial acceleration at the incident sidewall of the liner-fluid interface presents remarkable fluctuations. The liner-fluid interface is more sensitive to acceleration response than rock mass-liner interface under various radial elastic coefficients.

For the poor radial contact (e.g. K_r=μ_1/b and $0.1\mu_1/b$), Fig. 20 displays the circumferential stress variation at the two sidewalls and roof of

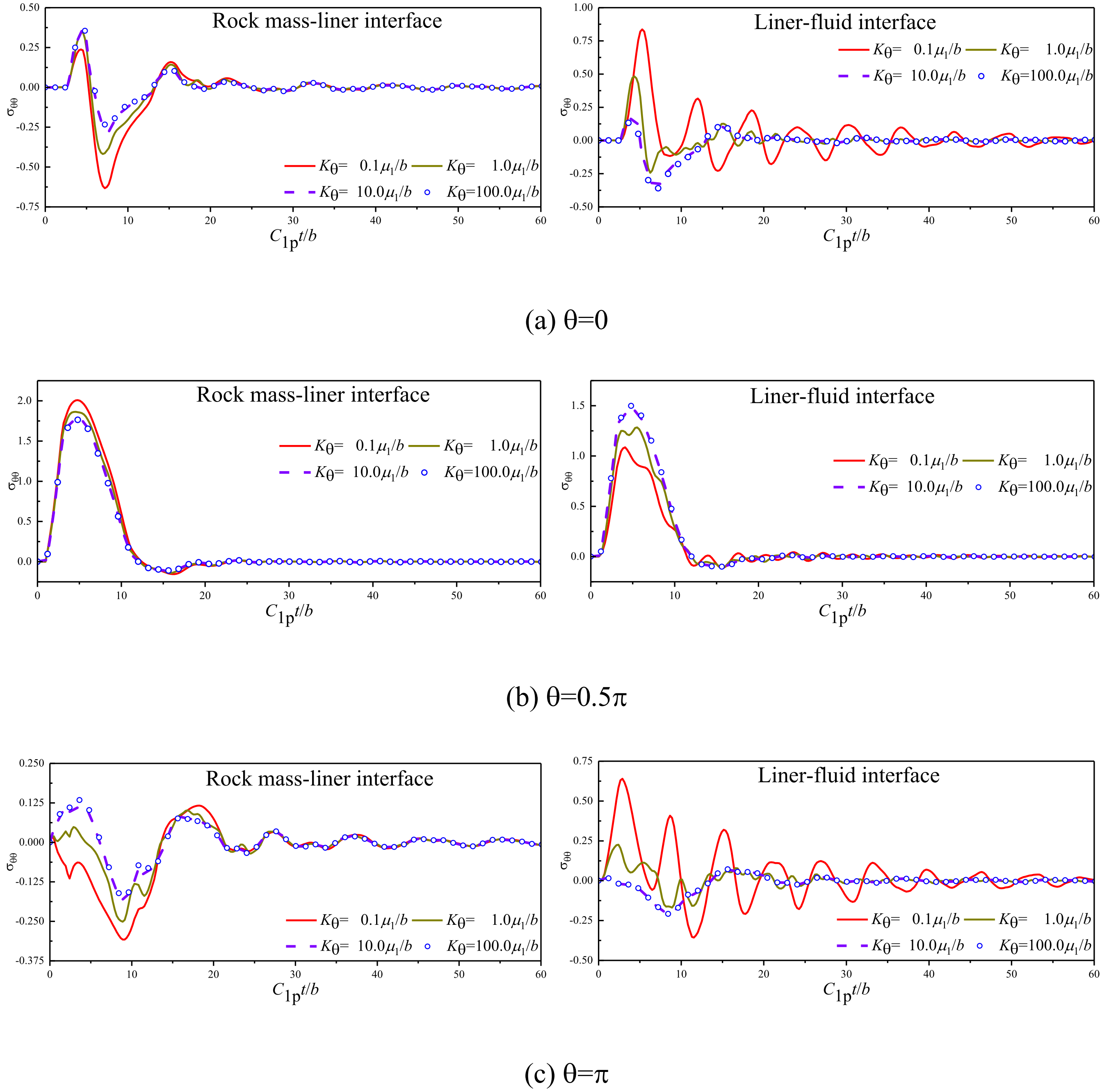

Fig. 14. The dimensionless circumferential stress variations at the rock mass-liner and liner-fluid interfaces under various K_θ.

the rock mass-liner and liner-fluid interfaces. It is identified that larger stress amplitude at the liner-fluid interface occurs along the disturbance direction, while larger peak stress at the rock mass-liner interface appears in regions perpendicular to the perturbation direction. The peak circumferential stress along the perturbation direction presents an increase as K_r decreases, and counterpart perpendicular to the disturbance direction exhibits an increase.

5.3. Effect of hoop elastic coefficient

For the case of K_r= 100μ_1/b and range of K_θ from 0.1μ_1/b to 100μ_1/b, Fig. 21 depicts the time-domain response of radial acceleration at the incident sidewall of the rock mass-liner and liner-fluid interfaces. It is observed from Fig. 21a that the radial acceleration at the incident sidewall of the rock mass-liner interface exhibits consistent variation without subtle fluctuations, immune to variation of hoop elastic coefficient. In contrast, as demonstrated in Fig. 21b, the radial acceleration at the incident sidewall of the liner-fluid interface presents prominent oscillations due to intricate mutual interaction. As illustrated in Fig. 22, reciprocating tensile and compressive stress concentrations induced by seismic P-wave appear around the diversion tunnel. The smaller hoop elastic coefficient is, the larger peak tensile and compressive stresses are and the more remarkable stress fluctuations along the disturbance direction occur, resulting in easier damage and failure of the surrounding rock and liner.

6. Conclusions

Based on the Laplace transform, the frequency-domain response of a deep-buried circular lined diversion tunnel with imperfect rock mass-

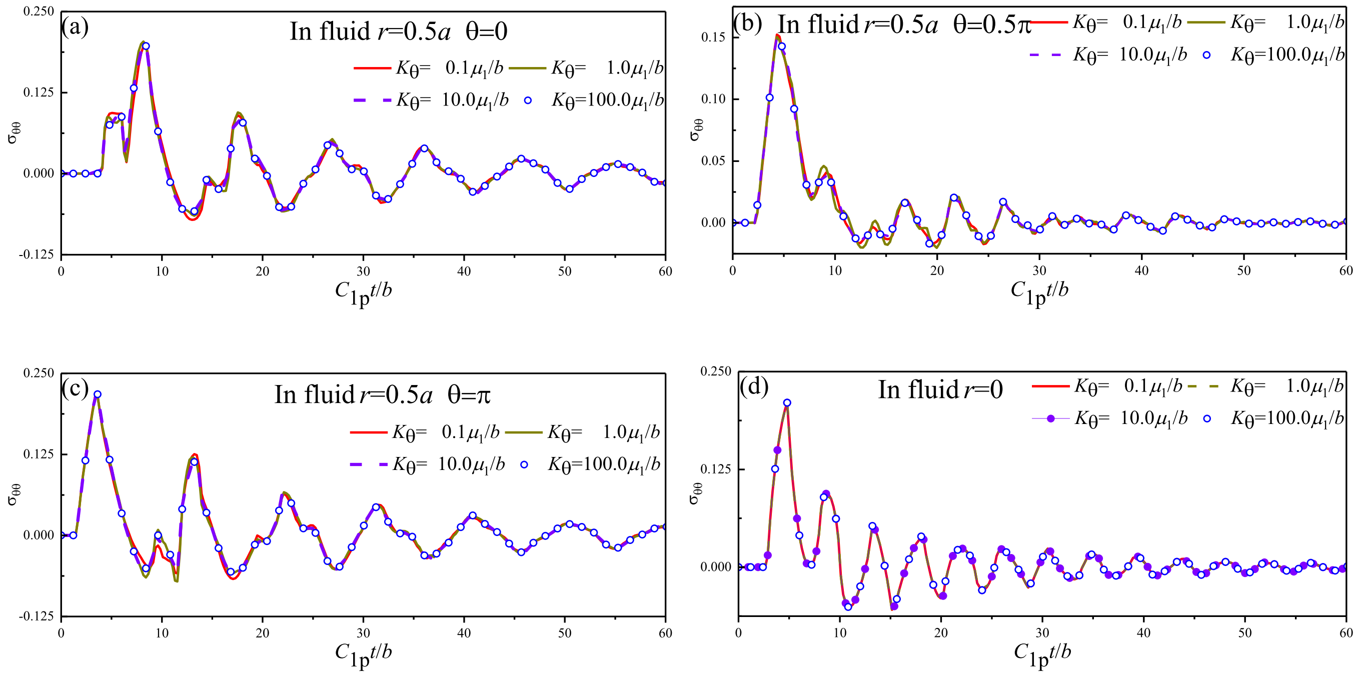

Fig. 15. The dimensionless fluid pressure response under various K_θ.

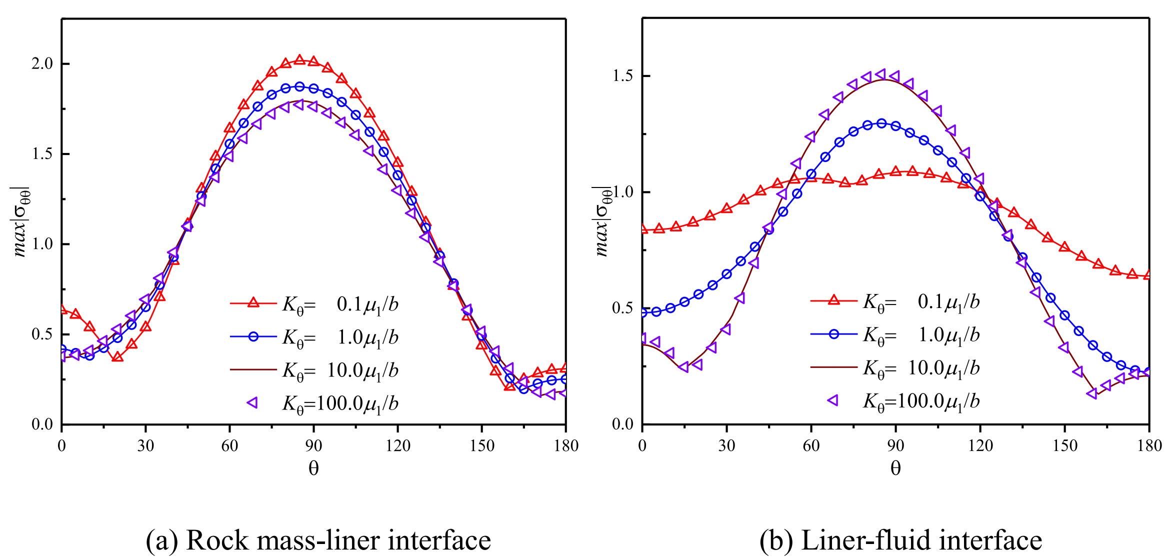

Fig. 16. Distributions of hoop stress at the rock mass-liner and liner-fluid interfaces under various K_θ.

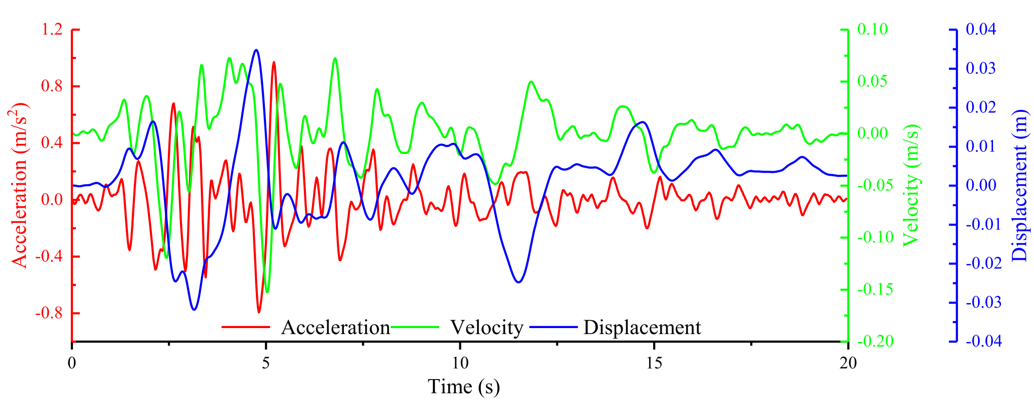

Fig. 17. Time-domain variation of incident seismic P-wave for acceleration, velocity and displacement.

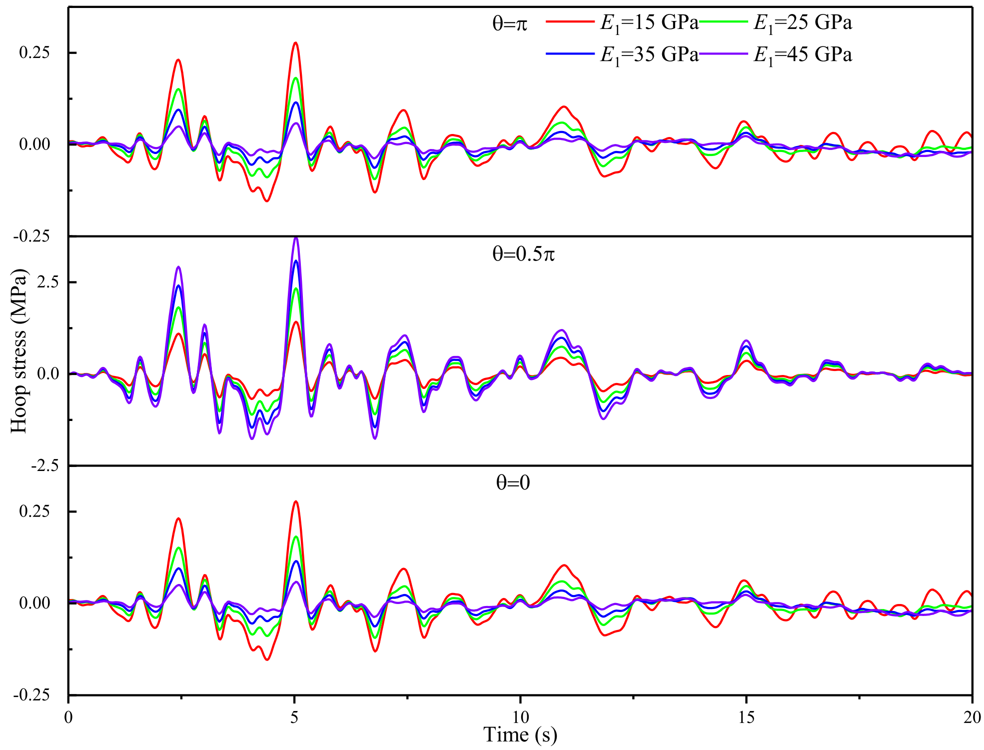

(a) Rock mass-liner interface

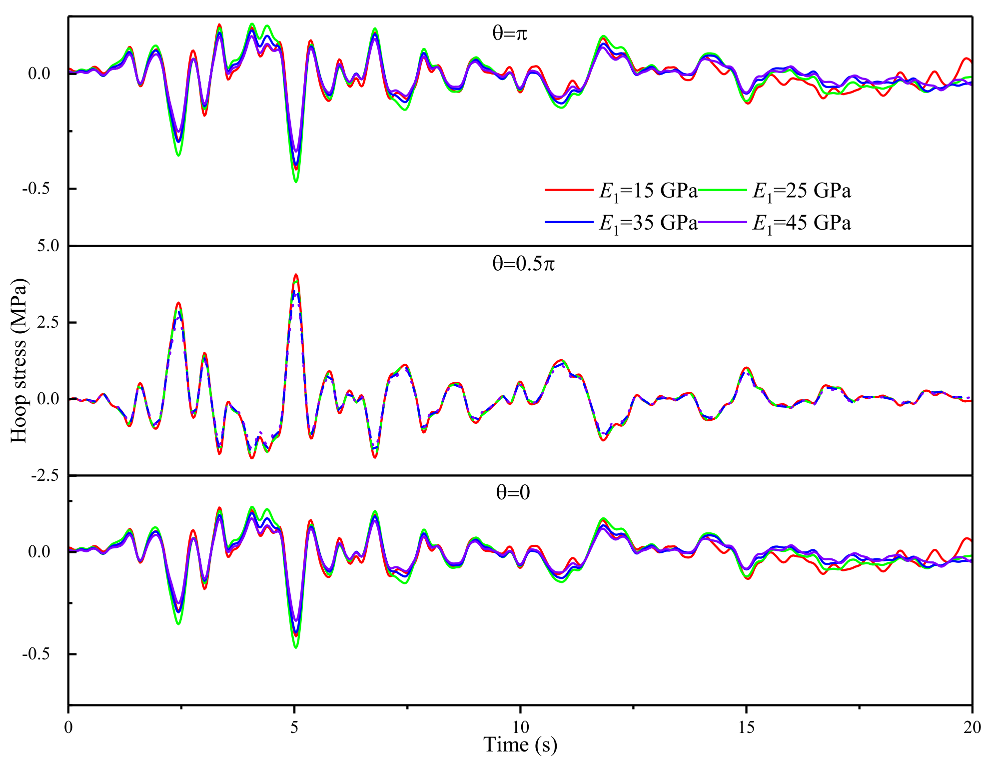

(b) Liner-fluid interface

Fig. 18. The time-history variations of tangent stress around the rock mass-liner and liner-fluid interfaces.

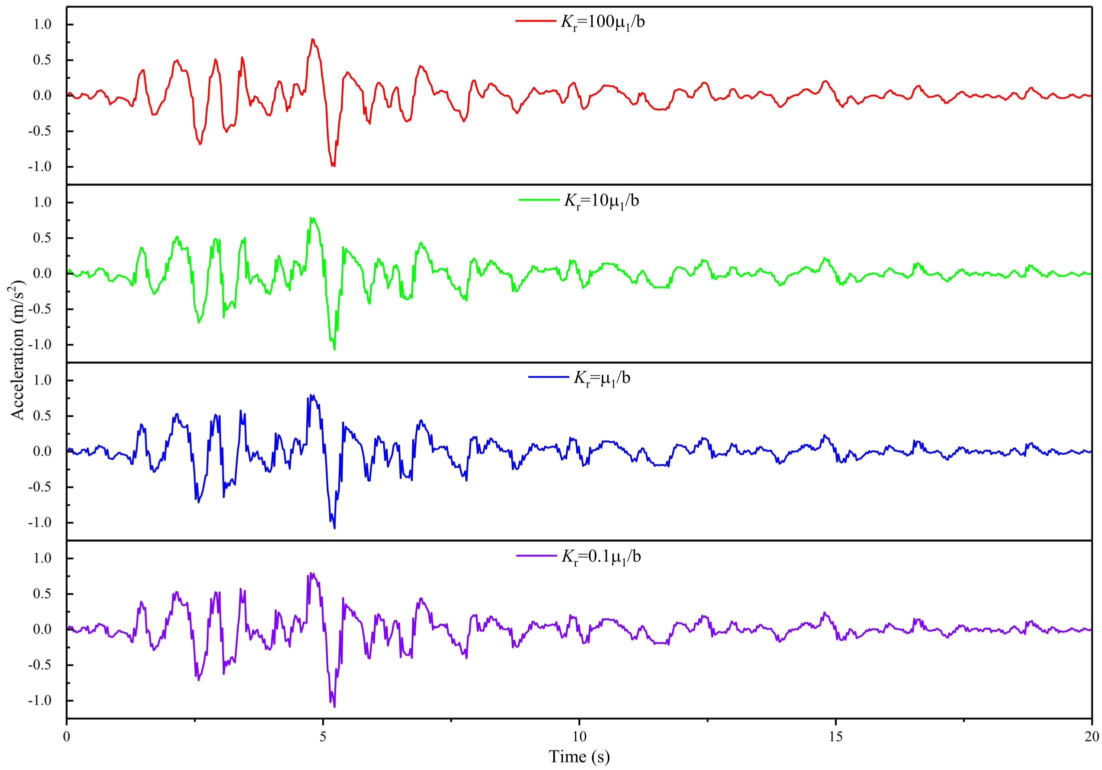

(a) Rock mass-liner interface

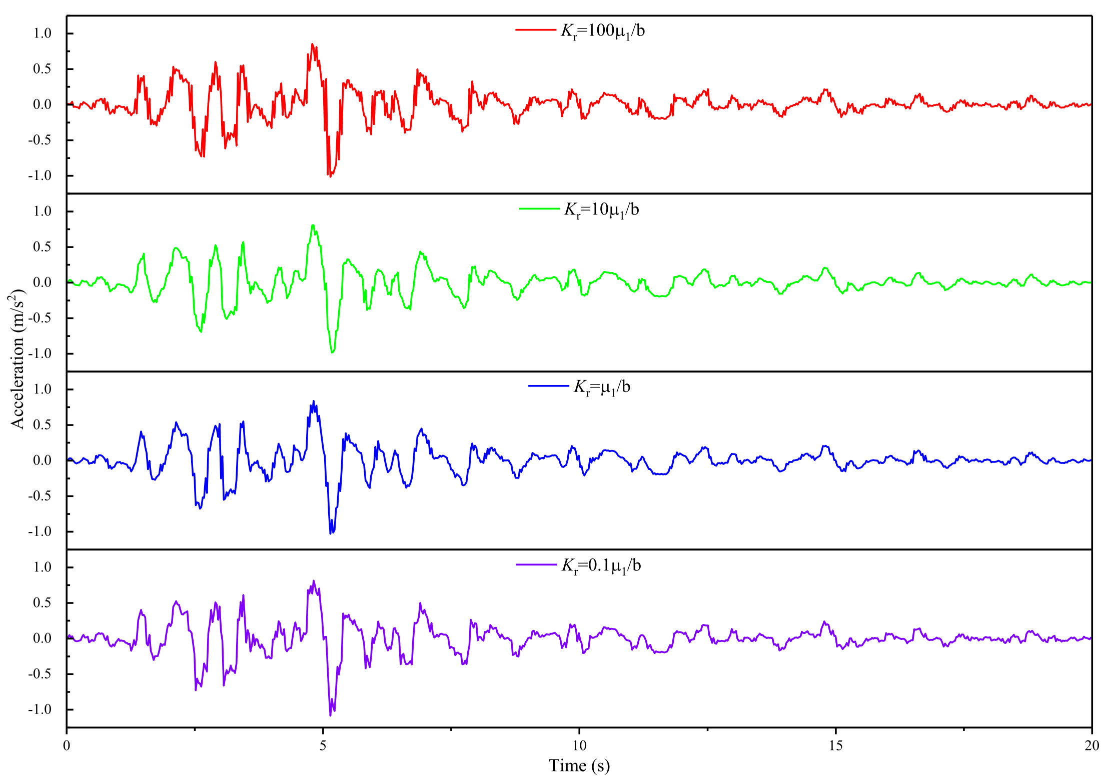

(b) Liner-fluid interface

Fig. 19. The time-history variations of radial acceleration at the incident sidewall around the rock mass-liner and liner-fluid interfaces under various K_r.

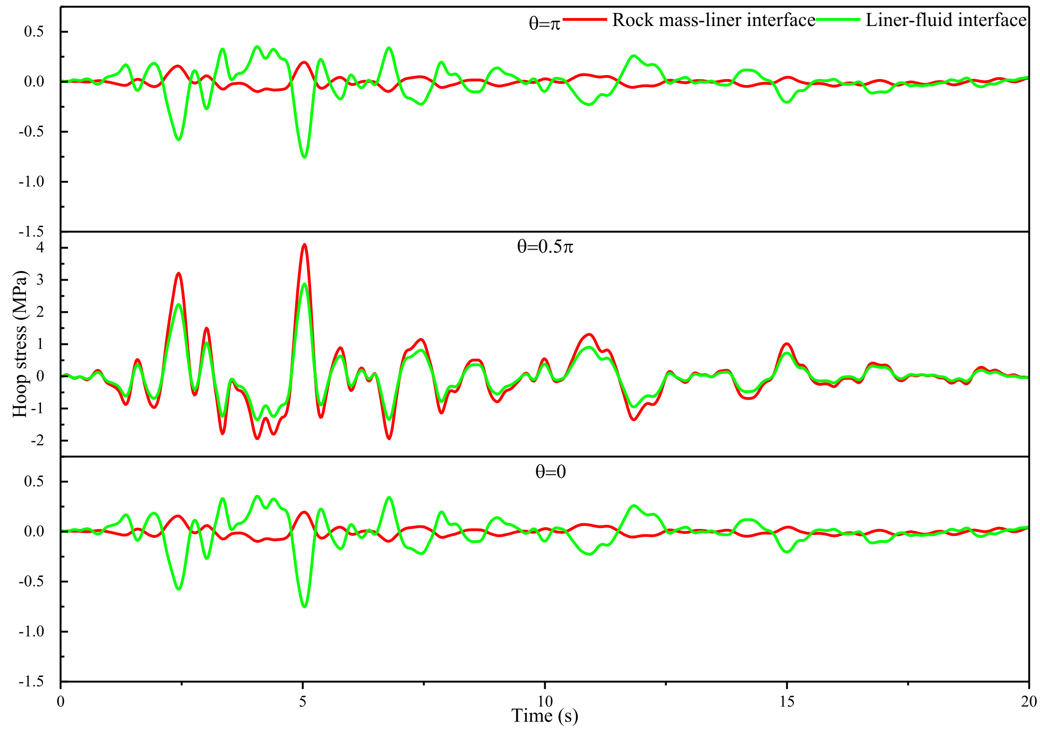

(a) K_r=μ₁/b

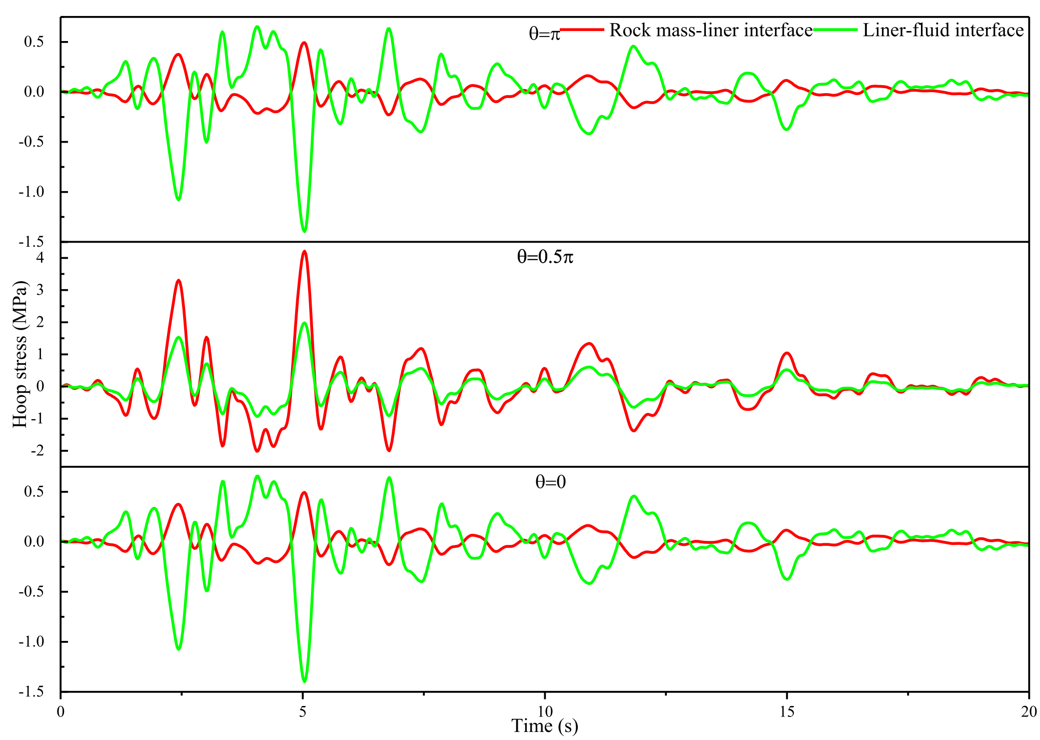

(b) K_r=0.1μ₁/b

Fig. 20. The time-history variations of circumferential stress around the rock mass-liner and liner-fluid interfaces.

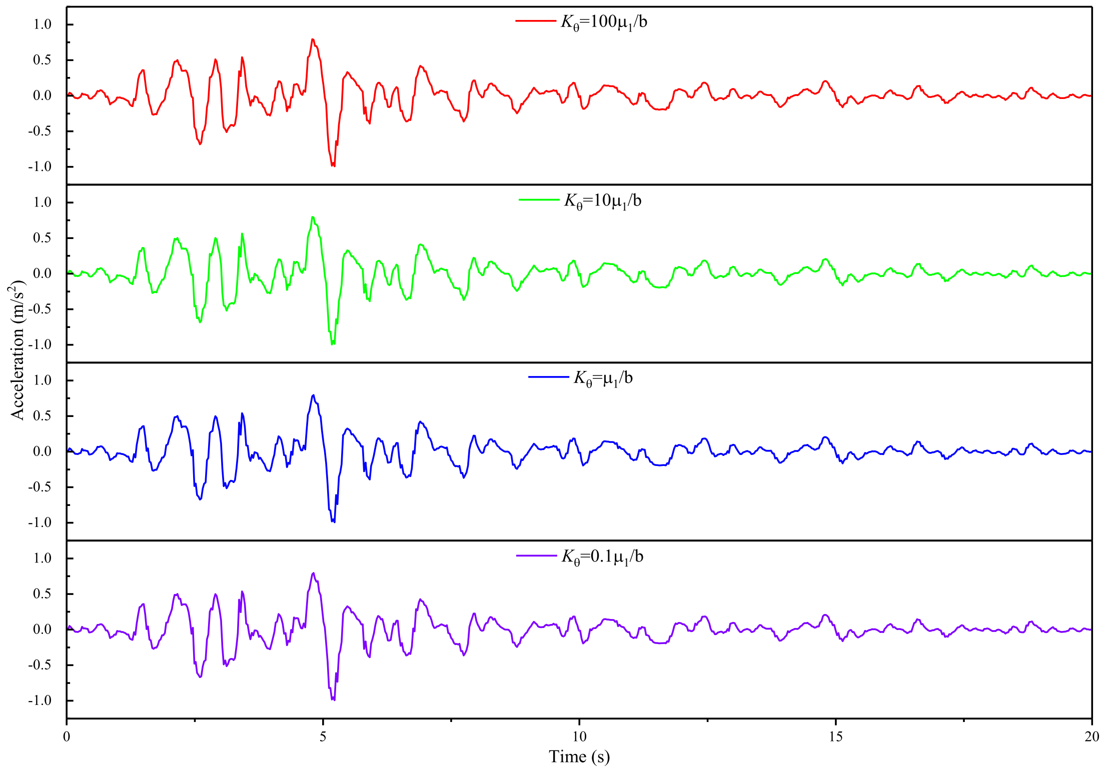

(a) Rock mass-liner interface

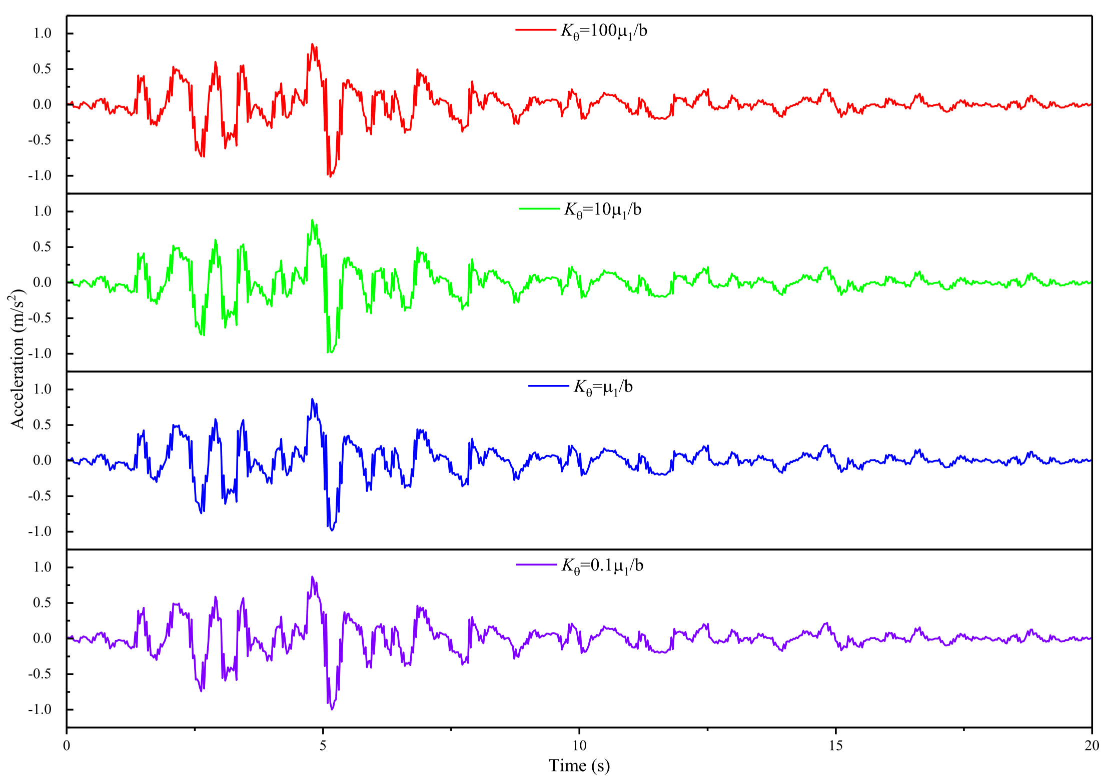

(b) Liner-fluid interface

Fig. 21. The time-history variations of radial acceleration at the incident sidewall around the rock mass-liner and liner-fluid interfaces under various K_θ.

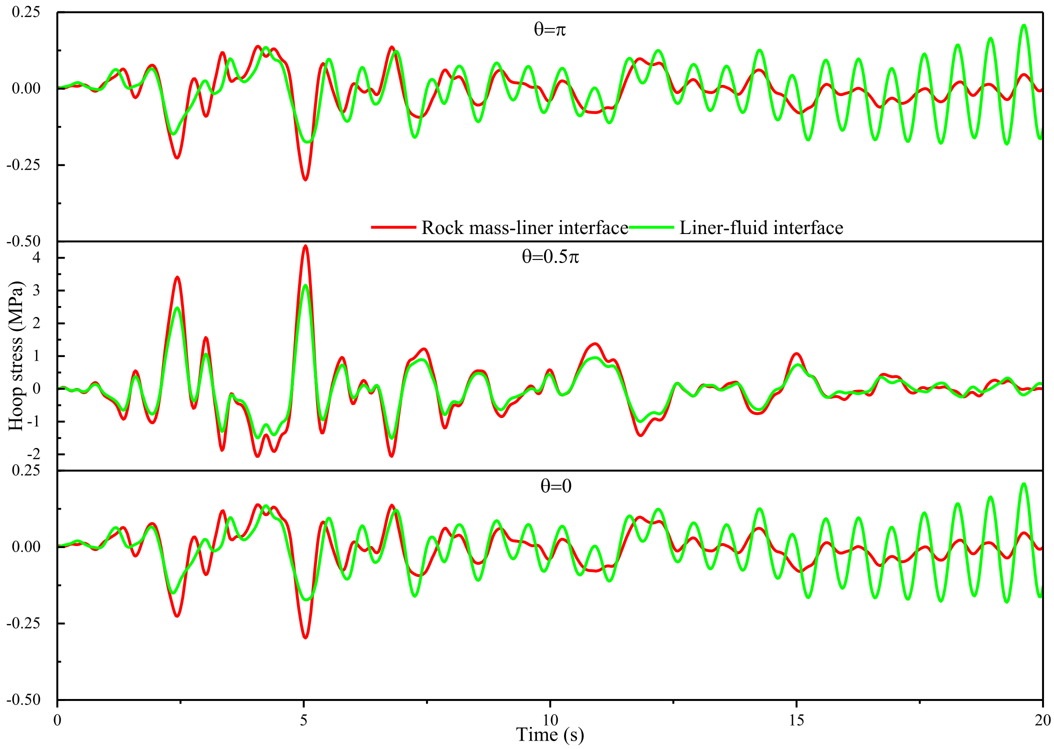

(a) $K_\theta=\mu_1/b$

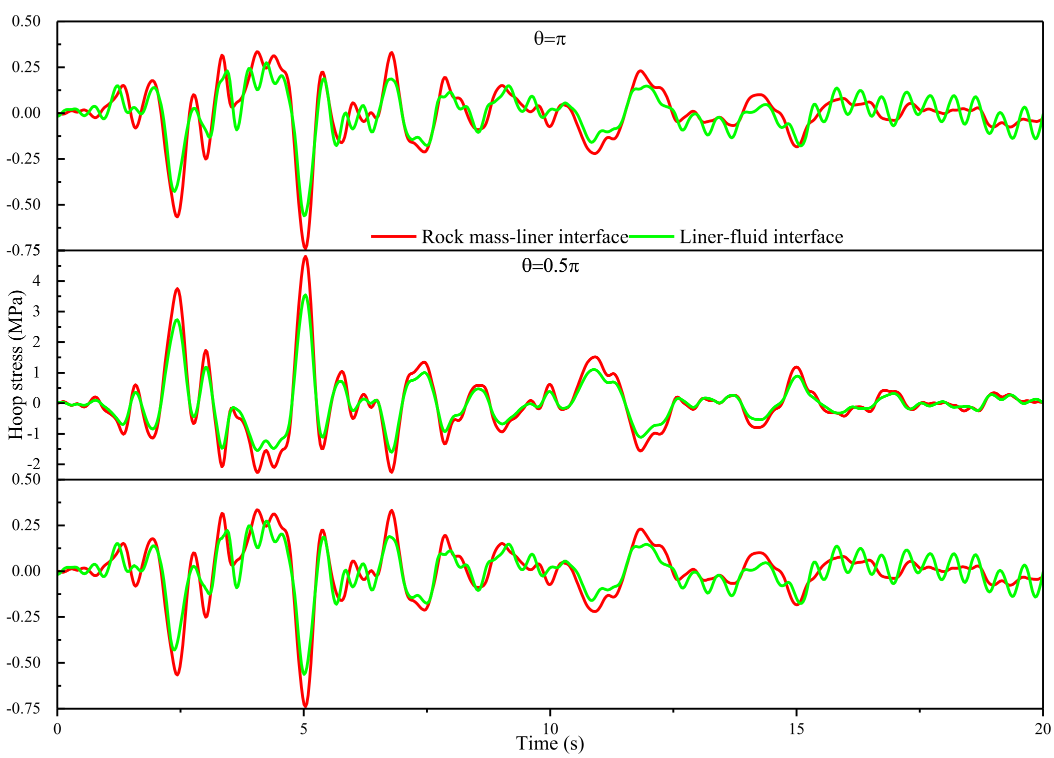

(b) $K_\theta=0.1\mu_1/b$

Fig. 22. The time-history variations of tangent stress around the rock mass-liner and liner-fluid interfaces.

liner interface under planar blasting or seismic P-wave was obtained. Then time-domain response of stress, acceleration, velocity and displacement components in solid and fluid domains was evaluated by the numerical inversion algorithm of Laplace transform. Several theoretical and numerical limitation cases were employed to verify the proposed methodology. The effects of elastic modulus of surrounding rock and interface parameters of the imperfect model on transient response induced by blasting and seismic P-waves were discussed. The following conclusions can be drawn:

(1) The scopes perpendicular to the perturbation direction generated pronounced dynamic compressive stress concentration induced by triangular blasting P-wave. The existence of fluid intensified the mutual interaction between stress wave and surrounding rock, liner and water, resulting in more remarkable stress and pressure fluctuations than an empty or a lined tunnel without fluid-filling.
(2) The rock mass-liner contact state had a significant influence on the transient response of surrounding rock, liner and water under blasting P-wave. The stress oscillation gradually deceased as the radial or hoop contact gradually improved. The radial contact remarkably affected dynamic response of water, while the transient response of fluid was immune to the hoop contact. The transient response around the diversion tunnel with imperfect interface converged to that with perfect contact when both K_{r} and K_{θ} exceeded $10\mu_1/b$.
(3) Scopes perpendicular to the disturbance direction generated more pronounced stress variation under seismic P-wave, special attention should be paid in practical engineering. The rock mass-liner interface under various radial elastic coefficients was more sensitive to acceleration response. The acceleration response around the liner-fluid interface presented remarkable fluctuations due to complex interaction.

The theoretical framework of this study is based on several fundamental and widely accepted assumptions, which make the complex wave-scattering problem analytically tractable. The surrounding rock and the liner are modeled as homogeneous, isotropic, linear elastic materials, while the internal fluid is assumed to be an inviscid, compressible ideal medium. Although these assumptions provide a clear and essential baseline model, they inherently exclude the investigation of several important real-world complexities, such as material saturation, nonlinearity, heterogeneity, anisotropy, and fluid viscosity. These simplifications define the scope of the present work and establish a necessary foundation. Future research will focus on extending the analysis to incorporate the effects of saturated porous medium in full- or half-space configurations, thereby enabling the study of transient response under more realistic geological and hydraulic conditions.

CRediT authorship contribution statement

Wanquan Mei: Writing – original draft, Software, Methodology, Funding acquisition. **Peng-Zhi Pan:** Supervision, Methodology, Funding acquisition. **Amin Hekmatnejad:** Validation, Methodology. **Zhaofeng Wang:** Validation, Software. **Yi Xie:** Writing – review & editing, Validation. **Qingsong Zheng:** Writing – review & editing.

Declaration of Competing Interest

The authors declare that they have no known competing financial interests or personal relationships that could have appeared to influence the work reported in this paper.

Acknowledgments

This work was supported by National Natural Science Foundation of China (Grant No. 52339001), China Postdoctoral Science Foundation (Grant No. 2025M773255) and Postdoctoral Fellowship Program of CPSF (Grant No. GZC20252069).

Appendix A

The detailed expressions of $\varepsilon_{ij}^{k}(\bullet)$ for displacement and stress components in the surrounding rock are expressed as

$$\varepsilon_{11}^{(1)}(\overline{k}_{1p}r) = (n^2 - n + 0.5\overline{k}_{1s}^2 r^2)I_n(\overline{k}_p r) - \overline{k}_{1p} r I_{n+1}(\overline{k}_{1p}r) \tag{A. 1}$$

$$\varepsilon_{11}^{(3)}(\overline{k}_{1p}r) = (n^2 - n + 0.5\overline{k}_{1s}^2 r^2)K_n(\overline{k}_{1p}r) + \overline{k}_{1p} r K_{n+1}(\overline{k}_{1p}r) \tag{A. 2}$$

$$\varepsilon_{12}^{(3)}(\overline{k}_{1s}r) = (n^2 - n)K_n(\overline{k}_{1s}r) - n\overline{k}_{1s} r K_{n+1}(\overline{k}_{1s}r) \tag{A. 3}$$

$$\varepsilon_{21}^{(1)}(\overline{k}_{1p}r) = \left(- n^2 + n + 0.5\overline{k}_{1s}^2 r^2 - \overline{k}_{1p}^2 r^2\right)I_n(\overline{k}_{1p}r) + \overline{k}_{1p} r I_{n+1}(\overline{k}_{1p}r) \tag{A. 4}$$

$$\varepsilon_{21}^{(3)}(\overline{k}_{1p}r) = \left(- n^2 + n + 0.5\overline{k}_{1s}^2 r^2 - \overline{k}_{1p}^2 r^2\right)K_n(\overline{k}_{1p}r) - \overline{k}_{1p} r K_{n+1}(\overline{k}_{1p}r) \tag{A. 5}$$

$$\varepsilon_{22}^{(3)}(\overline{k}_{1s}r) = (-n^2 + n)K_n(\overline{k}_{1s}r) + n\overline{k}_{1s} r K_{n+1}(\overline{k}_{1s}r) \tag{A. 6}$$

$$\varepsilon_{41}^{(1)}(\overline{k}_{1p}r) = (-n^2 + n)I_n(\overline{k}_{1p}r) - n\overline{k}_{1p} r I_{n+1}(\overline{k}_{1p}r) \tag{A. 7}$$

$$\varepsilon_{41}^{(3)}(\overline{k}_{1p}r) = (-n^2 + n)K_n(\overline{k}_{1p}r) + n\overline{k}_{1p} r K_{n+1}(\overline{k}_{1p}r) \tag{A. 8}$$

$$\varepsilon_{42}^{(3)}(\overline{k}_{1s}r) = (- n^2 + n - 0.5\overline{k}_{1s}^2 r^2)K_n(\overline{k}_{1s}r) - \overline{k}_{1s} r K_{n+1}(\overline{k}_{1s}r) \tag{A. 9}$$

$$\varepsilon_{71}^{(1)}(\overline{k}_{1p}r) = nI_n(\overline{k}_{1p}r) + \overline{k}_{1p} r I_{n+1}(\overline{k}_{1p}r) \tag{A. 10}$$

$$\varepsilon_{71}^{(3)}(\overline{k}_{1p}r) = nK_n(\overline{k}_{1p}r) - \overline{k}_{1p} r K_{n+1}(\overline{k}_{1p}r) \tag{A. 11}$$

$$\varepsilon_{72}^{(3)}(\overline{k}_{1s}r) = nK_n(\overline{k}_{1s}r) \tag{A. 12}$$

$$\varepsilon_{81}^{(1)}\left(\bar{k}_{1p}r\right) = -nI_n\left(\bar{k}_{1p}r\right) \tag{A. 13}$$

$$\varepsilon_{81}^{(3)}\left(\bar{k}_{1p}r\right) = -nK_n\left(\bar{k}_{1p}r\right) \tag{A. 14}$$

$$\varepsilon_{82}^{(3)}(\bar{k}_{1s}r) = -nK_n(\bar{k}_{1s}r) + \bar{k}_{1s}rK_{n+1}(\bar{k}_{1s}r) \tag{A. 15}$$

The detailed expressions of $\varepsilon_{ij}^{k}(\bullet)$ for displacement and stress components in the liner are expressed as

$$\varepsilon_{11}^{(4)}\left(\bar{k}_{2p}r\right) = \left(n^2 - n + 0.5\bar{k}_{2s}^2r^2\right)I_n\left(\bar{k}_{2p}r\right) - \bar{k}_{2p}rI_{n+1}\left(\bar{k}_{2p}r\right) \tag{A. 16}$$

$$\varepsilon_{11}^{(3)}\left(\bar{k}_{2p}r\right) = \left(n^2 - n + 0.5\bar{k}_{2s}^2r^2\right)K_n\left(\bar{k}_{2p}r\right) + \bar{k}_{2p}rK_{n+1}\left(\bar{k}_{2p}r\right) \tag{A. 17}$$

$$\varepsilon_{12}^{(4)}(\bar{k}_{2s}r) = \left(n^2 - n\right)I_n(\bar{k}_{2s}r) + n\bar{k}_{2s}rI_{n+1}(\bar{k}_{2s}r) \tag{A. 18}$$

$$\varepsilon_{12}^{(3)}(\bar{k}_{2s}r) = \left(n^2 - n\right)K_n(\bar{k}_{2s}r) - n\bar{k}_{2s}rK_{n+1}(\bar{k}_{2s}r) \tag{A. 19}$$

$$\varepsilon_{21}^{(4)}\left(\bar{k}_{2p}r\right) = \left(-n^2 + n + 0.5\bar{k}_{2s}^2r^2 - \bar{k}_{2p}^2r^2\right)I_n\left(\bar{k}_{2p}r\right) + \bar{k}_{2p}rI_{n+1}\left(\bar{k}_{2p}r\right) \tag{A. 20}$$

$$\varepsilon_{21}^{(3)}\left(\bar{k}_{2p}r\right) = \left(-n^2 + n + 0.5\bar{k}_{2s}^2r^2 - \bar{k}_{2p}^2r^2\right)K_n\left(\bar{k}_{2p}r\right) - \bar{k}_{2p}rK_{n+1}\left(\bar{k}_{2p}r\right) \tag{A. 21}$$

$$\varepsilon_{22}^{(4)}(\bar{k}_sr) = \left(-n^2 + n\right)I_n(\bar{k}_sr) - n\bar{k}_srI_{n+1}(\bar{k}_sr) \tag{A. 22}$$

$$\varepsilon_{22}^{(3)}(\bar{k}_{2s}r) = \left(-n^2 + n\right)K_n(\bar{k}_{2s}r) + n\bar{k}_{2s}rK_{n+1}(\bar{k}_{2s}r) \tag{A. 23}$$

$$\varepsilon_{41}^{(4)}\left(\bar{k}_{2p}r\right) = \left(-n^2 + n\right)I_n\left(\bar{k}_{2p}r\right) - n\bar{k}_{2p}rI_{n+1}\left(\bar{k}_{2p}r\right) \tag{A. 24}$$

$$\varepsilon_{41}^{(3)}\left(\bar{k}_{2p}r\right) = \left(-n^2 + n\right)K_n\left(\bar{k}_{2p}r\right) + n\bar{k}_{2p}rK_{n+1}\left(\bar{k}_{2p}r\right) \tag{A. 25}$$

$$\varepsilon_{42}^{(4)}(\bar{k}_{2s}r) = \left(-n^2 + n - 0.5\bar{k}_{2s}^2r^2\right)I_n(\bar{k}_{2s}r) + \bar{k}_{2s}rI_{n+1}(\bar{k}_{2s}r) \tag{A. 26}$$

$$\varepsilon_{42}^{(3)}(\bar{k}_{2s}r) = \left(-n^2 + n - 0.5\bar{k}_{2s}^2r^2\right)K_n(\bar{k}_{2s}r) - \bar{k}_{2s}rK_{n+1}(\bar{k}_{2s}r) \tag{A. 27}$$

$$\varepsilon_{71}^{(4)}\left(\bar{k}_{2p}r\right) = nI_n\left(\bar{k}_{2p}r\right) + \bar{k}_{2p}rI_{n+1}\left(\bar{k}_{2p}r\right) \tag{A. 28}$$

$$\varepsilon_{71}^{(3)}\left(\bar{k}_{2p}r\right) = nK_n\left(\bar{k}_{2p}r\right) - \bar{k}_{2p}rK_{n+1}\left(\bar{k}_{2p}r\right) \tag{A. 29}$$

$$\varepsilon_{72}^{(4)}(\bar{k}_{2s}r) = nI_n(\bar{k}_{2s}r) \tag{A. 30}$$

$$\varepsilon_{72}^{(3)}(\bar{k}_{2s}r) = nK_n(\bar{k}_{2s}r) \tag{A. 31}$$

$$\varepsilon_{81}^{(4)}\left(\bar{k}_{2p}r\right) = -nI_n\left(\bar{k}_{2p}r\right) \tag{A. 32}$$

$$\varepsilon_{81}^{(3)}\left(\bar{k}_{2p}r\right) = -nK_n\left(\bar{k}_{2p}r\right) \tag{A. 33}$$

$$\varepsilon_{82}^{(4)}(\bar{k}_{2s}r) = -nI_n(\bar{k}_{2s}r) - k_{2s}rI_{n+1}(\bar{k}_{2s}r) \tag{A. 34}$$

$$\varepsilon_{82}^{(3)}(\bar{k}_{2s}r) = -nK_n(\bar{k}_{2s}r) + \bar{k}_{2s}rK_{n+1}(\bar{k}_{2s}r) \tag{A. 35}$$

Appendix B

The detailed element expressions of coefficient matrix R are represented by

$$R_{1,1} = -\frac{\mu_1}{\mu_2}E_{11}^{(3)}\left(\bar{k}_{1p}b\right),\ R_{1,2} = -\frac{\mu_1}{\mu_2}E_{12}^{(3)}(\bar{k}_{1s}b),\ R_{1,3} = E_{11}^{(3)}\left(\bar{k}_{2p}b\right) \tag{B. 1}$$

$$R_{1,4} = E_{11}^{(4)}\left(\bar{k}_{2p}b\right),\ R_{1,5} = E_{12}^{(3)}(\bar{k}_{2s}b),\ R_{1,6} = E_{12}^{(4)}(\bar{k}_{2s}b),\ R_{1,7} = 0 \tag{B. 2}$$

$$R_{2,1} = -\frac{\mu_1}{\mu_2}E_{41}^{(3)}\left(\bar{k}_{1p}b\right),\ R_{2,2} = -\frac{\mu_1}{\mu_2}E_{42}^{(3)}(\bar{k}_{1s}b),\ R_{2,3} = E_{41}^{(3)}\left(\bar{k}_{2p}b\right) \tag{B. 3}$$

$$R_{2,4} = E_{41}^{(4)}\left(\bar{k}_{2p}b\right),\ R_{2,5} = E_{42}^{(3)}(\bar{k}_{2s}b),\ R_{2,6} = E_{42}^{(4)}(\bar{k}_{2s}b),\ R_{2,7} = 0 \tag{B. 4}$$

$$R_{3,1} = -E_{71}^{(3)}\left(\bar{k}_{1p}b\right) + \frac{2\mu_1}{bK_r}E_{11}^{(3)}\left(\bar{k}_{1p}b\right),\ R_{3,2} = -E_{72}^{(3)}(\bar{k}_{1s}b) + \frac{2\mu_1}{bK_r}E_{12}^{(3)}(\bar{k}_{1s}b) \tag{B. 5}$$

$$R_{3,3} = E_{71}^{(3)}\left(\overline{k}_{2p}b\right),\ R_{3,4} = E_{71}^{(4)}\left(\overline{k}_{2p}b\right),\ R_{3,5} = E_{72}^{(3)}(\overline{k}_{2s}b),\ R_{3,6} = E_{72}^{(4)}(\overline{k}_{2s}b) \tag{B. 6}$$

$$R_{3,7} = 0,\ R_{4,7} = 0 \tag{B. 7}$$

$$R_{4,1} = -E_{81}^{(3)}\left(\overline{k}_{1p}b\right) + \frac{2\mu_1}{bK_\theta}E_{41}^{(3)}\left(\overline{k}_{1p}b\right),\ R_{4,2} = -E_{82}^{(3)}(\overline{k}_{1s}b) + \frac{2\mu_1}{bK_\theta}E_{42}^{(3)}(\overline{k}_{1s}b) \tag{B. 8}$$

$$R_{4,3} = E_{81}^{(3)}\left(\overline{k}_{2p}b\right),\ R_{4,4} = E_{81}^{(4)}\left(\overline{k}_{2p}b\right),\ R_{4,5} = E_{82}^{(3)}(\overline{k}_{2s}b),\ R_{4,6} = E_{82}^{(4)}(\overline{k}_{2s}b) \tag{B. 9}$$

$$R_{5,1} = 0,\ R_{5,2} = 0,\ R_{5,3} = E_{11}^{(3)}\left(\overline{k}_{2p}a\right),\ R_{5,4} = E_{11}^{(4)}\left(\overline{k}_{2p}a\right) \tag{B. 10}$$

$$R_{5,5} = E_{12}^{(3)}(\overline{k}_{2s}a),\ R_{5,6} = E_{12}^{(4)}(\overline{k}_{2s}a),\ R_{5,7} = -0.5 \times \left(\overline{k}_{2s}^{2}r\right)^{2}\rho_3\Big/\rho_2 I_n\left(\overline{k}_{3p}r\right) \tag{B. 11}$$

$$R_{6,1} = 0,\ R_{6,2} = 0,\ R_{6,3} = E_{41}^{(3)}\left(\overline{k}_{2p}a\right),\ R_{6,4} = E_{41}^{(4)}\left(\overline{k}_{2p}a\right) \tag{B. 12}$$

$$R_{6,5} = E_{42}^{(3)}(\overline{k}_{2s}a),\ R_{6,6} = E_{42}^{(4)}(\overline{k}_{2s}a),\ R_{6,7} = 0 \tag{B. 13}$$

$$R_{7,1} = 0,\ R_{7,2} = 0,\ R_{7,3} = E_{71}^{(3)}\left(\overline{k}_{2p}a\right),\ R_{7,4} = E_{71}^{(4)}\left(\overline{k}_{2p}a\right) \tag{B. 14}$$

$$R_{7,5} = E_{72}^{(3)}(\overline{k}_{2s}a),\ R_{7,6} = E_{72}^{(4)}(\overline{k}_{2s}a),\ R_{7,7} = -E_{71}^{(1)}\left(\overline{k}_{3p}a\right) \tag{B. 15}$$

Data availability statement

All data included in this study are available upon reasonable request by contact with the corresponding author.

References

[1] B.B. Sun, M.J. Deng, S.R. Zhang, et al., Inelastic dynamic analysis and damage assessment of a hydraulic arched tunnel under near-fault SV waves with arbitrary incoming angles, Tunn. Undergr. Space Technol. 104 (2020) 103523.

[2] B.B. Sun, S.R. Zhang, W. Cui, et al., Nonlinear dynamic response and damage analysis of hydraulic arched tunnels subjected to P waves with arbitrary incoming angles, Comput. Geotech. 118 (2020) 103358.

[3] P.F. Chen, Q. Jiang, J. Liu, et al., Global stability coefficient of large underground caverns under static loading and earthquake wave condition, J. Cent. South Univ. 31 (8) (2024) 2826–2843.

[4] F. Wang, Y.H. Xue, Y.Y. Zhang, et al., Response of existing lining subjected to closed blasting in zero-spacing twin tunnels and its damping measures, Eng. Fail. Anal. 166 (2024) 108847.

[5] X.T. Feng, H. Xu, S.L. Qiu, et al., In situ observation of rock spalling in the deep tunnels of the China Jinping Underground Laboratory (2400 m depth), Rock Mech. Rock Eng. 51 (4) (2018) 1193–1213.

[6] C. Mow, Y. Pao, The diffraction of elastic waves and dynamic stress concentration, Crane-Russak, NewYork, 1971.

[7] Z.F. Fan, J.C. Zhang, H. Xu, Theoretical study of the dynamic response of a circular lined tunnel with an imperfect interface subjected to incident SV-waves, Comput. Geotech. 110 (2019) 308–318.

[8] Y. Tan, M.S. Yang, X.Y. Li, Dynamic response of a circular lined tunnel with an imperfect interface embedded in the unsaturated poroelastic medium under P wave, Comput. Geotech. 122 (2020) 103514.

[9] C.P. Yi, P. Zhang, D. Johansson, et al., Dynamic response of a circular lined tunnel with an imperfect interface subjected to cylindrical P-waves, Comput. Geotech. 55 (2014) 165–171.

[10] C.P. Yi, W.B. Lu, P. Zhang, et al., Effect of imperfect interface on the dynamic response of a circular lined tunnel impacted by plane P-waves, Tunn. Undergr. Space Technol. 51 (2016) 68–74.

[11] S.M. Hasheminejad, R. Avazmohammadi, Dynamic stress concentrations in lined twin tunnels within fluid-saturated soil, J. Eng. Mech. 134 (7) (2008) 542–554.

[12] E. Zlatanović, V. Šešov, D.Č. Lukić, et al., Influence of a new-bored neighbouring cavity on the seismic response of an existing tunnel under incident P- and SV-waves, Earthq. Eng. Struct. Dyn. 50 (11) (2021) 2980–3014.

[13] D.K. Liu, B.Z. Gai, G.Y. Tao, Applications of the method of complex functions to dynamic stress concentrations, Wave Motion 4 (3) (1982) 293–304.

[14] H. Bouaré, A. Mesgouez, G. Lefeuve-Mesgouez, Stress and displacement fields around an arbitrary shape tunnel surrounded by a multilayered elastic medium subjected to harmonic waves under plane strain conditions, Soil Dyn. Earthq. Eng. 154 (2022) 107158.

[15] Z.G. Chen, Application of least square method to solve the scattering of plane P-wave on a cavity, Earthq. Eng. Eng. Vib. 39 (6) (2019) 106–112 (in Chinese).

[16] X. Wang, X.P. Zhang, Dynamic stress concentration of a non-circular cavern in a viscoelastic medium subjected to a plane P-wave, Acta Mech. 233 (4) (2022) 1455–1466.

[17] Y.T. Si, J.P. Liu, F. Li, et al., Experimental and theoretical investigation of roadway fracture induced by static-blast loading using acoustic emission, Eng. Fail. Anal. 143 (2023) 106909.

[18] Z.X. Liu, H. Zhang, A. Cheng, et al., Seismic interaction between a lined tunnel and a hill under plane SV waves by IBEM, Int. J. Struct. Stab. Dyn. 19 (2) (2019) 1950004.

[19] Y. Xu, Q.H. Han, Z.X. Liu, et al., The diffraction of rayleigh waves by twin circular cavities in a poroelastic half-space, J. Earthq. Eng. 22 (5) (2018) 970–987.

[20] Y.B. Yang, H.H. Hung, K.C. Lin, et al., Dynamic response of elastic half-space with cavity subjected to P and SV waves by finite/infinite element approach, Int. J. Struct. Stab. Dyn. 15 (7) (2015) 1540009.

[21] M. Li, Y.J. Lu, W.Q. Mei, et al., Analytical solution and influencing factors of dynamic response of deep-buried diversion tunnel with circular composite lining under transient disturbance by P-wave, Blasting 42 (2) (2025) 22–30 (in Chinese).

[22] X.B. Li, C.J. Li, W.Z. Cao, et al., Dynamic stress concentration and energy evolution of deep-buried tunnels under blasting loads, Int. J. Rock Mech. Min. Sci. 104 (2018) 131–146.

[23] M. Tao, Z.W. Li, W.Z. Cao, et al., Stress redistribution of dynamic loading incident with arbitrary waveform through a circular cavity, Int. J. Numer. Anal. Methods Geomech. 43 (6) (2019) 1279–1299.

[24] W.Q. Mei, Y.Y. Xia, P.Z. Pan, et al., Influence of wavelength-to-excavation span ratio on dynamic failure characteristics of a deep-buried tunnel subjected to disturbance, Int. J. Geomech. 22 (10) (2022) 04022170.

[25] W.Q. Mei, Y.Y. Xia, P.Z. Pan, et al., Transient responses of deep-buried unlined tunnels subjected to blasting P wave, Comput. Geotech. 146 (2022) 104729.

[26] Y.Y. Xia, G.S. Han, W.Q. Mei, et al., Dynamic responses of a shallow lined tunnel with imperfect interface under transient P wave, Int. J. Struct. Stab. Dyn. 24 (17) (2023) 2450187.

[27] W.Q. Mei, Y.Y. Xia, P.Z. Pan, et al., Transient wave-induced dynamic responses of a circular composite-lined tunnel with imperfect interface, Waves Random Complex Media 35 (7) (2026) 13208–13230.

[28] R. Shakeri, A. Mesgouez, G. Lefeuve-Mesgouez, Transient response of a concrete tunnel in an elastic rock with imperfect contact, Int. J. Min. Sci. Technol. 30 (5) (2020) 605–612.

[29] C.J. Li, X.B. Li, Influence of wavelength-to-tunnel-diameter ratio on dynamic response of underground tunnels subjected to blasting loads, Int. J. Rock Mech. Min. Sci. 112 (2018) 323–338.

[30] X.Q. Fang, T.F. Zhang, B.L. Li, et al., Elastic-slip interface effect on dynamic stress around twin tunnels in soil medium subjected to blast waves, Comput. Geotech. 119 (2020) 103301.

[31] M. Tao, G.L. Xiang, R. Zhao, et al., Scattering of P-wave and transient response around a fluid-filled cavity in an elastic medium, J. Cent. South Univ. 30 (2) (2023) 568–583.

[32] W.Q. Mei, P.Z. Pan, A. Hekmatnejad, et al., Theoretical and numerical responses of deep-buried diversion twin tunnels with imperfect interfaces under blasting or seismic P- and SV-waves, Soil Dyn. Earthq. Eng. 201 (2026) 109964.
[33] H. Alielahi, M. Adampira, Effect of twin-parallel tunnels on seismic ground response due to vertically in-plane waves, Int. J. Rock Mech. Min. Sci. 85 (2016) 67–83.
[34] H. Alielahi, M. Adampira, Seismic effects of two-dimensional subsurface cavity on the ground motion by BEM: Amplification patterns and engineering applications, Int. J. Civ. Eng. 14 (4) (2016) 233–251.
[35] P. Kavandi, M. Panji, N. Ganjian, et al., An alternative dual reciprocity BEM for P-SV wave propagation problems: A comparative study, Eng. Anal. Bound. Elem. 176 (2025) 106238.
[36] M. Panji, S. Mojtabazadeh-Hasanlouei, Seismic ground response by twin lined tunnels with different cross sections, SN Appl. Sci. 3 (9) (2021) 787.
[37] H. Luo, M. Tao, Z.X. Hong, et al., Analysis of the dynamic response and damage characteristic for the tunnel under near-field blasts and far-field earthquakes, Undergr. Space 21 (2025) 331–351.
[38] G.L. Xiang, M. Tao, R. Zhao, et al., Dynamic response of water-rich tunnel subjected to plane P wave considering excavation induced damage zone, Undergr. Space 15 (2024) 113–130.
[39] R. Zhao, M. Tao, G.L. Xiang, et al., Blasting induced dynamic stress concentration and failure characteristics of deep-buried rock tunnel, J. Cent. South Univ. 31 (7) (2024) 2321–2340.
[40] C. Cao, X.Q. Fang, C.S. Zhu, Effects of a semi-circular valley on dynamic response of shallow tunnel with imperfect interface under Rayleigh wave incidence, Soil Dyn. Earthq. Eng. 190 (2025) 109204.
[41] J. Toutain, J.L. Battaglia, C. Toutain, et al., Numerical inversion of laplace transform for time resolved thermal characterization experiment, J. Heat Transf. 133 (4) (2011) 044504.
[42] N. Al-Ajmi, M. Ahmadi, E. Ozkan, et al., Numerical inversion of Laplace transforms in the solution of transient flow problems with discontinuities, in: SPE Annual Technical Conference and Exhibition, Denver, Colorado, USA, 2008.
[43] P. den Iseger, Numerical transform inversion using Gaussian quadrature, Probab. Eng. Inf. Sci. 20 (1) (2006) 1–44.
[44] F.H. Escobar, F.A. Leguízamo, J.H. Cantillo, Comparison of Stehfest's and Iseger's algorithms for Laplacian inversion in pressure well tests, ARPN J. Eng. Appl. Sci. 9 (4) (2014) 919–922.
[45] Q. Feng, B.S. Jiang, G. Wang, et al., Analytical solution for a circular roadway considering the transient effect of excavation unloading, Int. J. Min. Sci. Technol. 26 (4) (2016) 543–549.
[46] W.Q. Mei, Y.Y. Xia, G.S. Han, et al., Theoretical responses of shallow-buried circular cavity subjected to transient P wave, Comput. Geotech. 139 (2021) 104411.
[47] M. Li, W.Q. Mei, P.Z. Pan, et al., Modeling transient excavation-induced dynamic responses in rock mass using an elasto-plastic cellular automaton, Tunn. Undergr. Space Technol. 96 (2020) 103183.
[48] W.Q. Mei, P.Z. Pan, M. Li, et al., Modelling transient unloading-triggered dynamic responses in rock mass under a non-hydrostatic geo-stress, Comput. Geotech. 175 (2024) 106672.

Dr. Wanquan Mei received his Ph.D. degree at the school of Civil Engineering and Architecture, Wuhan University of technology, Wuhan, China. His research interests are in the dynamic response of deep rock, rock damage mechanics, wave propagation, blasting, and tunneling. He develops dynamic version of Cellular Automata Software for engineering Rock-mass fracturing process (CASRock), focusing on the application of advanced theoretical and numerical methods to investigate the dynamic response of surrounding rock. He published more than 20 technical papers in *Computers and Geotechnics, Tunneling and Underground Space Technology, Soil Dynamics and Earthquake Engineering, International Journal of Geomechanics, Geophysical Journal International*, etc.